Size-dependent strength and plasticity in nanocrystalline metal with amorphous intergranular films

By

Afzal Hossain Neelav

A Thesis submitted to the Faculty of Graduate Studies of

the University of Manitoba

in partial fulfillment of the requirements for the degree of

Master of Science

Department of Mechanical Engineering

University of Manitoba

Winnipeg, Manitoba

Abstract

Grain boundaries are important in polycrystalline materials as they control the overall microstructural evolution and serve as both sinks and sources for dislocation activities in the material. Substituting crystalline atoms at the grain boundary region with amorphous intergranular films, it is possible to enhance dislocation absorption and so, reduce crack nucleation and growth at the interface. In this study, we have used Molecular Dynamics simulations to investigate the interface energy and their deformation mechanism under various mechanical loading of bi-crystal and polycrystal copper with the amorphous intergranular film. We have found that the presence of amorphous intergranular films reduces the interface energy and orientation dependence cannot be observed anymore. We have investigated both the effects of grain size (3 nm to 17 nm) and amorphous intergranular film thicknesses (0.5 nm to 1.5 nm). We have found a strong effect of the amorphous intergranular films in the strength of the material by causing a shift in the strongest grain size to a larger size. Moreover, we have found changes in the deformation mechanism due to the presence of the amorphous intergranular films from dislocation mechanism to grain boundary activity. Finally, thermal stability has been observed in the nanocrystalline copper with amorphous intergranular films during high-temperature creep.

Acknowledgment

I would like to show my deepest gratitude towards my supervisor, Dr. Chuang Deng from the Department of Mechanical Engineering, who was patient, helpful, instructive and kind during my education. Dr. Deng provided me with a suitable opportunity to work on materials science, and without his support, I would not be able to finish this work.

In addition, I would like to thank and appreciate the committee members, Dr. Xihui Liang from the Department of Mechanical Engineering and Dr. Mohamed Bassuoni from the Department of Civil Engineering. Thank you for reviewing my thesis and attending the defense. And I would also like to give thanks to my colleagues and friends in my research group who supported all the time.

Last but not least, I would like to thank my wife, my family for their help and support and my friends who encouraged me to overcome the obstacles and finish my graduation.

Dedication

Dedicated to my beloved soulmate, Kaniz, for her unconditional generous support and love in my life.

Table of contents

Table of figures

Abbreviations

GB/GBs	Grain boundary/Grain boundaries
CSL	Coincidence lattice site
AIF/AIFs	Amorphous intergranular film/films
NC	Nanocrystalline
PC	Polycrystalline
NW	Nanowire
MD	Molecular Dynamics
HP	Hall-Petch
IHPE	Inverse Hall-Petch effect
PBC	Periodic boundary condition
EAM	Embedded atomic potential
LAMMPS	Large-scale atomic/molecular massively parallel simulator

CHAPTER 1 Introduction

1.1. Motivation

Nanocrystalline (NC) materials are defined as materials having an average grain size from a few to 100 nm. NC materials demonstrate unique mechanical and physical properties like high hardness [1] and fatigue resistance [2] along with an order of magnitude increment in the strength leading them to an utmost interest for a wide range of applications. [3]–[10] These unique properties owe to their special structural features like a dramatic increment in the volume fraction of the material at the grain boundaries (GBs) due to the grain refinement. [11], [12] In spite of possessing these superior material properties, NC materials have two major limitations which might be connected to the preponderance of GBs: (a) lack of ductility, and (b) limited thermal stability. Therefore, researchers have been trying to find a way to overcome these limitations in order to utilizing the NC materials to its fullest potential. [13], [14]

GB complexion is a general concept; the amorphous interfacial film (AIF) is just one type of GB complexion. [15]–[17] [18] It has been proposed that the AIF can be used as a nanostructuring method for the prolonged tradeoff between strength and ductility by improving both properties at the same time. For the first time, this AIF has been introduced in a Cu-Zr system with a one-dimensional pillar which made it first of its kind. Researchers have found experimentally that the presence of the AIF not only improved the toughness of the material but also lead a way in the improvement of thermal stability. [19] For our research, we would like to explore the size effect of the AIF in the same Cu-Zr system; specially in the bulk material. Again, it would be interesting to investigate whether the fundamental mechanism of deformation could be changed due to this

new GB restructuring to AIF. By finding these answers, it can open the door for more bulk materials and might be also possible to predict more novel properties of the NC materials in future.

Experimental techniques provide valuable insights corresponding to the different aspects of material science, but it comes with the expense of expensive facilities. Sometimes it is challenging to analyze the specimen without ignoring the practical issues. As a result, atomistic simulations have been used vastly to study the GB deformation process and other related phenomena due to its accuracy, flexibility and economic efficiency. In this thesis, the proposed method to investigate the effect of AIFs is molecular dynamics (MD) simulation.

1.2. Objective

In this thesis, MD simulations are used to study the effect of the AIF in both bi-crystal and NC materials. This research has three primary objectives:

- To investigate the effect of the AIF on the interfacial energy of bi-crystal Cu
- To study if there is size effect by varying both grain sizes and AIF thicknesses when the regular interface is substituted with the AIF.
- To understand the role of AIF in the deformation mechanism in NC metals.

1.3. Outline

In chapter 2, we present a thorough literature review. This chapter begins with the introductory information on NC metals, their deformation process, and their mechanical properties. Then it reviews the GB complexion, how GB complexion affects the deformation mechanism of the NC metals and the latest approach by introducing this complexion in the GB region to improve the strength and ductility of NC metals.

In chapter 3, we explain the complete methodology used in performing the simulations during this research work. We describe the models, the MD method and all the parameters that have been used in this work.

In chapter 4, we explain the result of this research work including the effect of the AIF in the energy of bi-crystal Cu, the influence of the AIF in the deformation mechanism in the NC models with different grain size and GB widths and corresponding discussions.

In chapter 5, we summarize the whole work and conclude the results with some future work suggestions.

CHAPTER 2 Literature review

2.1 GBs

2.1.1. Structure of GBs

The interface between two crystallites or grains of the same material with different orientations in a crystalline material in a manner that material is continuous across this interface is called GB. [20] Five macroscopic parameters are needed to describe the geometry of a GB uniquely. Among them, three macroscopic parameters in a cubic system are the rotational axis cosines [u v w] (two parameters) and the rotation angle θ(one parameter); the other two define the normal of the interface plane. [21]

With this terminology a GB is said to be tilt if the axis of rotation [u v w] is in the plane of GB, it is twisted if the rotation axis [u v w] is perpendicular to GB plane and if the rotation axis is inclined, the GB is called mixed. On the other hand, if the plane between two grains can be expressed by$\{h\ k\ l\}_1 = \{h\ k\ l\}_2$, the boundary is called symmetric otherwise it is asymmetric. [21] Schematic diagrams of different GBs are shown in Figure 2-1.

The figure has been removed due to copyright issues

Figure 2-1: GBs based on relative orientation and rotation axes. (a) Twist boundary; (b) symmetric tilt boundary, and (c) asymmetric tilt boundary [21]

2.1.2. GB energy

GB energy is the amount of work required to create one unit of GB through a thermodynamic process. In other words, GB energy per unit is, γ, is the excess free energy per unit area that exists in the system due to the presence of the GB. GB energy is a function of thermodynamic parameters like temperature (T), pressure (P), the chemical potential (μ_i) or composition. [22] The lowest

energy can be achieved when two adjacent grains have the same orientation, *i.e.*, there is no GB between them. By rotating one grain relative to the other, the energy increases, but there are some special angles of rotation, for which the energy is a local minimum. [23] The reason behind this lower energy is that there are some sites on GB which coincide with both adjacent grains. Figure 2-2 shows the variation in GB energy with respect to misorientation angle between the grains.

The figure has been removed due to copyright issues

Figure 2-2: Dependence of the energy of symmetric ⟨110⟩ tilt boundaries in Al on the tilt angle Φ. The indices given in the figure are Miller indices of the corresponding GB planes. [24]

These special sites where the GB energy becomes minimum are known as coincidence site lattice (CSL). [21] CSL theory describes the formation of these special GBs. Based on this theory, the misorientation angle between two grains cannot be any arbitrary value since the free energy becomes high and the material tends to decrease it, so the misorientation angle should be a local minimum to be stable. To measure the coincidence sites, a parameter Σ has been defined which is the ratio of volume cell of CSL to the volume cell of the crystal lattice.

$$\Sigma = \frac{Volume\ cell\ of\ CSL}{Volume\ cell\ of\ crystal\ lattice} \qquad (2-1)$$

From Figure 2-3, we can see a schematic diagram for CSL in Σ=5 and Σ=3 in a bi-crystal.

The figure has been removed due to copyright issues

Figure 2-3: Coincidence lattice unit cells viewed along the rotation axis (a) of a Σ=5 bi-crystal: rotation around the 001 axis in a body-centered cubic (bcc) lattice; (b) of a Σ=3 bi-crystal: rotation

around 011 in a face-centered cubic (fcc) lattice (here four coincidence cells are represented). The common points of the lattices are bicolored. Different point sizes indicate different positions along the normal to the scheme. The projection of the crystalline lattices is indicated by dashed lines. [21]

2.2. NC materials

NC materials consist of single or multi-phase polycrystals at the nanoscale regime. Usually, they fall in the range of 1 x 10^{-9} to 250 x 10^{-9} m. [2] This material has been a subject of widespread research over the past couple of decades because of their potential in numerous applications. [25]–[29] NC materials contain a large volume fraction of atoms at the GBs.

Palumbo et al.[3] first showed that approximately 30% of the material is located in the GB region for an average grain size of 10 nm. Figure 2-4 shows the increment in volume fraction of atoms with the reduction of grain size.

The figure has been removed due to copyright issues

Figure 2-4: Volume fraction vs. grain size curve. [3]

It leads to high strength-to-weight ratios for this material. As a result, their physical, mechanical and chemical properties are much different compared to conventional coarse-grained PC materials. [30], [31]

2.2.1. Plasticity in conventional PC materials and Hall-Petch (HP) relation

Plastic deformation of coarse-grained PC materials is generally mediated by the nucleation and motion of dislocations-line defects of the regular crystal lattice. Under mechanical loading,

multiple dislocations generate in the slip planes so that dislocation motion can easily occur and lead to plastic deformation. In other words, during plastic deformation, dislocations must be primarily generated in these slip planes. As a result of the mechanical loading, these generated dislocations move through the crystalline lattice, *i.e.* the grains till they come across a different GB. [32] As GBs are a collection of large atomic disorder, a GB region results in a discontinuity of slip planes from one grain to another. Therefore, a cluster of dislocations piles up together at the GB. The amount of dislocation pile-up increases when the grain size is decreased because of the greater total GB area. As a result, higher applied stress is required to move the dislocations leading to higher yield strength. Thus, there is an inverse relationship between yield stress and grain size which is described by the famous HP equation: [33]

$$\sigma_y = \sigma_o + \frac{k_y}{\sqrt{d}} \qquad (2\text{-}2)$$

Here, σ_y is the yield stress, σ_o is materials constant for initial stress to nucleate dislocations, k_y is a constant specific to each material and d is the average grain diameter. Due to the HP effect, NC materials have been established as high-hardness materials. Moreover, the HP effect is believed to be outcome of the GBs hindering dislocation activity and thereby, making the plastic deformation more difficult at smaller grain sizes. [34]

The figure has been removed due to copyright issues

Figure 2-5: Atomistic simulation structure of a PC material with a grain diameter of 49 nm after 10% deformation. [34]

From Figure 2-5, we can see how the deformation behavior for PC material is governed by dislocations. Here, blue atoms are the perfect face-centered-cubic crystalline grains; yellow atoms exhibit stacking faults, and red ones are the atoms in GBs and dislocation cores. From this atomistic structure, it was stated that new dislocations were generated at the GBs, propagated through the grains and absorbed at other GBs.

While strength can be dramatically increased by decreasing grain sizes to nanoscale, the ductility of these materials is disappointingly low. For a typical NC material, ductility can be as low as 2% elongation, whereas, conventional grain size metals exhibit a large 40% to 60% elongation, showing higher ductility.

The figure has been removed due to copyright issues

Figure 2-6: Engineering stress vs. engineering strain curve of NC Cu and coarse-grained Cu showing the trade-off between strength and ductility. The inset figure shows the stress-strain curve for consolidated NC Cu. [35]

From Figure 2-6, we can clearly find the difference in both strength and ductility between NC Cu and coarse-grained Cu. The coarse-grained Cu offers higher elongation at the expanse of lower strength. On the other hand, NC Cu shows much higher strength with the limitation of ductility. Therefore, lack of ductility has been the biggest drawback of NC materials with lower grain sizes despite having numerous potentials in applications due to their hardness and yield strength.

2.2.2. HP breakdown and plasticity in NC metals

The plastic deformation of coarse-grained metals at a relatively low temperature is governed by the nucleation and motion of dislocations. As grain refinement continues, dislocation activity

eventually becomes very difficult to occur. With the increment in the volume fraction of interfaces, GB activities might become more effective and the material becomes softer with further decrease in the grain size. This effect is known as inverse Hall-Petch effect (IHPE). Wadsworth and Nieh [36] first predicted that HP relationship would break in various materials after a critical grain size. As the grain sizes become smaller, they can not withhold more than one dislocation. They proposed a critical equilibrium spacing between dislocation l_c when the HP relationship will not work anymore.

$$l_c = \frac{3Gb}{\pi(1-v)H} \qquad (2\text{-}3)$$

According to this theory, if the grain size is smaller than $l_{c,}$ then there will be no dislocation pile-ups and result in the breakdown of the HP relationship. Typically, this phenomenon is expected to occur for grain sizes below 20 nm for most metals. [36], [37] In experiments, it was for the first time reported by Choksi et al. [38] that negative HP slope could be found at the room temperature for Cu and Pd. This researcher explained these new phenomena citing two reasons: 1. GB creep occurs at a high rate compared to coarse-grained polycrystalline materials; 2. GB diffusion is more like to occur because of smaller grain size. Some other experimental measurements have also shown various deviations from the HP equation. [39], [40]

Along with the softening, the plasticity in the NC materials below the critical size (~ 15 nm to 20 nm) deviate from the conventional theories. Regarding the deformation mechanism, it was first proposed by Swyngenhoven et al. [11] that when the grain size is reduced to below a certain values (~15 nm to 20 nm) GB-mediated plasticity (e.g., GB sliding and/or grain rotation) substitutes the conventional dislocation nucleation and motion as the dominant deformation mechanism. Another research from Schiotz et al. [41] also showed that most of the plastic

deformation in NC materials is due to the large number of sliding events of atomic planes at the GBs, with a minor part being caused by dislocation activity in the grains.

2.2.2.1. GB sliding

GB sliding is the dominant process in the plasticity of NC materials when the grain size is below 15 nm. [42]

Figure 2-6 shows a schematic diagram where one layer of grains slide with respect to the other by producing a shear strain in the process. Plastic deformation has taken place through the translation of the top layer of grains with respect to the bottom layer of grains.

The figure has been removed due to copyright issues

Figure 2-6: GB sliding model; (a) initial position of grains; (b) top layer position after sliding [42]

Van Swygenhoven et al. [43] performed MD simulations to reveal sliding along boundaries and showed that GB sliding is the primary deformation mechanism in NC materials below 15 nm

The figure has been removed due to copyright issues

Figure 2-7: Sectional view of a GB is exhibiting the sliding of the upper grain (grain 14) relative to the lower grain (grain 1) accompanied by atomic shuffling across the GB. (displacement vectors show the change in positions of the atoms) [11]

From Figure 2-7, we can see the GB sliding occurring between two grains. It was shown that GB sliding includes a significant amount of atomic activity either by shuffling of individual atoms or shuffling between several atoms with a degree of correction. Since the presence of excess free

volume in the GB region plays an important role in this mechanism, therefore GB sliding is facilitated by both atomic shuffling and stress-assisted free volume migration. [11]

2.2.2.2. GB rotation

Ma and coworkers [44]–[46] first pointed out the interesting point that nanosized grains rotate during plastic deformation and they can coalesce along directions of shear and thus, create a larger path for dislocation movement. This mechanism can lead to the softening of the material. If the orientations of two neighboring grain match with each other, then the barrier between them, *i.e.*, the boundary is eliminated and provide a path for more dislocation motion. Figure 2-8 shows a schematic diagram exhibiting the steps in GB rotation.

The figure has been removed due to copyright issues

Figure 2-8**:** Rotation of neighboring grains during plastic deformation and creation of elongated grain by removal of adjacent GB. [46]

Wang et. al. [47] showed experimentally that for grain size below 6 nm, the plastic deformation mode turns into grain rotation by involving multiple grains in a collective manner.

2.2.3. Thermo-stability of NC metals

One of the shortcomings of NC material is the lack of thermal stability. [48]–[50] As GBs are like all defects, they contain excess free energy associated with the deviation from the original or preferred crystalline arrangement of atoms. As a result, NC materials have a large driving force to coarsen their grain structure as they tend to reduce the interfacial area inside the materials. Therefore, pure or elemental NC materials exhibit grain growth to a significant level even at room temperature. [48] Thus, this loss of thermal stability becomes an obstacle for the practical

production of NC materials. This problem can be addressed either by the thermodynamic or kinetic approach. [51] Thermodynamic strategies focus on the thermal stability by reducing the driving force for grain growth. Weissmuller et al. [52], [53] suggested that adding dopants in the GB could lead a reduction in the GB energy to almost zero and thus, totally get rid of the driving force for the grain growth. On the contrary, kinetic strategies prefer to reduce the mobility of the GB atoms by adding dopants or by introducing a secondary phase to restrict the movement of the interface. [54], [55] However, between these two approaches, the thermodynamic approach has the upper hand because it mostly removes the problem of grain growth whereas, kinetic approaches might break down at high temperatures.

2.3.GB complexion

As we have discussed in the previous sections that despite possessing superior material properties, NC materials have two major limitations which are (i) limited thermal stability and (ii) lack of ductility due to HP effects. To obtain a solution of these problems, researchers gave an idea that tailoring the structure of GB by changing interfacial chemistry may be able to delay the damage nucleation for the NC materials. It has been recognized that GB changes their intrinsic properties like structure, chemistry concerning the change of thermodynamic parameters such as temperature, pressure, chemical potential. [57] As the interface states can be treated thermodynamically, therefore, a new term ‘complexion’ has been introduced to differentiate between the interfacial state to its abutting thermodynamic phase. [18] Till now, complexions have been investigated and implemented in either coarse-grained PC materials or simple bi-crystal samples. A recent strategy has shown that by segregating dopant atoms, GB can be tailored to obtain local equilibrium structure and thus, use the concept of complexion to overcome the

limitations of NC materials. This specific process is termed as GB complexion engineering. We will discuss about the types of GB complexion and their effect in the following sections.

2.3.1. GB complexion in pure and non-pure metals

The very first work demonstrating the complexion of GB reported by Hart et al. [21] exhibited complexion stability for two distinct regions and their transition line in a P-T diagram.

The figure has been removed due to copyright issues

Figure 2-9: An early theoretical GB complexion diagram for a pure material showing the pressure-temperature (P–T) locus of a complexion transition between two hypothetical complexions, complexion a (blue region) and complexion b (red region) [56]

Figure 2-9 is a schematics diagram showing a transition between two distinct complexions, which are complexion α (blue region) and complexion β (pink region), both depicting low-temperature and high-temperature GB phase respectively. From that onwards, there have been several types of research to understand how the parameters such pressure (P) and temperature (T) play a role in the complexion as well as if these parameters can be measured experimentally. But all these GBs complexion transitions in pure materials consider fixed grain shape and geometrical parameters to describe the GB. These types of complexion transition are known as 'congruent' transitions. Experimentally, they can be only characterized by changes in the atomic structure in the GB region. However, in experiments, most of the materials contain impurities, and essentially, congruent transitions occur rarely in a non-pure system. These non-congruent or dissociative types of complexion are known as 'wetting transition'.

GB segregation/adsorption is the most crucial factor in a complexion transition of a non-pure metal. Early theories for GBs adsorption mostly assumed of a monolayer system. [57] However,

later, a demonstration of adsorption in multiple layers was found accompanied by key changes in the structure of a GB.

Figure 2-10: MD and Monte Carlo simulation results that demonstrate intrinsic (a–c) and extrinsic (d, e) GB complexion transitions at a Σ5(310) boundary in pure Cu (a–c) and Ag-doped Cu (d, e) [56]

Figure 2-10 shows the difference between intrinsic and extrinsic GB complexion transition at a Σ5 (310) boundary in both pure Cu (a-c) and a doped system of Ag-Cu (d-e). From Figure (a-c), during congruent complexion transition, two different boundaries coexist and meet at a single, one-dimensional complexion boundary. The structures at the GB region generally known as (c) kites and (d) split kites. On that contrary, when this same boundary of Cu is doped with Ag, two completely different structures can be observed which is called ‘monolayer’ and ‘bilayer’. [18]

2.3.2. Discrete complexions

GB complexions can be categorized by their width regarding the number of atomic layers. Dillon and Harmer [58] studied grain growth kinetics on doped alumina with high -angle annular dark field scanning transmission electron microscopy (HAADF-STEM) to distinguish between distinct types of GB complexions.

Figure 2-11: The six discrete Dillon–Harmer complexions as originally discovered in undoped and doped (CaO, MgO, SiO2, Nd2O3) Al2O3 (a–f) and analogous examples of discrete Dillon–Harmer complexions in metallic systems. [58], [59]

As shown in the Figure 2-11, all the discrete complexions can be classified into six categories based on their thickness, and these are known as Dillon-Harmer complexion categorization framework. In addition to our previous discussion on monolayer and bilayer, nanolayer complexions are greater than three layers in thickness, approximately on the order of one or two nanometers in thickness. This nanolayer is also known as Intergranular films (IGF). The final one, wetting, is a different one compared to others in this category. It is more like a bulk phase rather than a complexion. While all the others have a fixed and finite thickness, wetting has an arbitrary thickness. However, it was suggested by this researcher that even though this framework help to categorize between different complexions; it is not necessary that all the nanolayers must have the same thickness. It is possible to have a single type of nanolayer complexion within a given system as well as there might be multiple types of nanolayers with different thicknesses in a particular system. These complexions can be classified in another way based on their recognizable periodicity. It can be an ordered periodicity which types I to IV from Dillon-Harmer complexion. On the other hand, if the complexion lack ordered periodicity and exhibit long-range order, they can be regarded as type V and VI.

2.3.3. AIF; a GB complexion form

As discussed in the previous section, complexion type V and VI often exhibit long-range crystalline order, in which both of them can be considered as AIFs. AIF is an example of GB complexion that is both distinct in its local structure as well as its effect on material properties. Amorphous materials were firstly considered for an ideal candidate because of their excess free

volume. This idea was exhibited by Wang et al. [60] by introducing copper-zirconium NC-amorphous nanolaminates. They applied multiple stress-relaxation cycles on their sample and found that deformation occurs at a much lower stress level in NC-amorphous nanolaminate compared to the crystalline-crystalline nanolaminates. Further research by the same group showed with computational simulations that it is possible to achieve an almost elastic-perfectly plastic behavior without necking. [61] They explained this behavior due to the presence of amorphous atoms in the GBs as this new phase acts as high capacity sinks for dislocations and so enabling them to show unique inelastic slip transfer characteristics. An atomistic simulation on the same nanolaminate system performed by Brandl et al. [62] showed that the interfacial shear of the amorphous-crystalline interface attracts several dislocations as well as increase their absorptions. Another research performed on NC-amorphous composites containing 37% crystalline phase by M. Falk et al. [63] found deformation initiation at the amorphous phase by shear bands and these bands being blocked at the crystalline interface. However, all these studies used amorphous metal as the major phase and therefore, leads to the formation of shear banding. Unfortunately, due to the heavy presence of amorphous phase, these models tend to show limited ductility despite having higher flow stress.

2.3.4. Formation of AIF

Till date, AIF has been studied and implemented predominantly in either coarse-grained PC materials or simple bi-crystals. The first experimental report on a strategy for combining both the concepts of nanostructuring and GB complexion engineering was provided by Rupert et al. [19] For this experiment, this researcher used Cu-based alloys since Cu is a common face-centred cubic material and deformation mechanism and properties of pure NC Cu material have been well studied. Zr was picked as the alloying element, as it segregates to the GB easily and binary Cu-Zr

alloys have a high glass forming ability. [64], [65] A high-energy ball milling technique was used to create a Cu-3 atomic % Zr alloy. To diffuse the Zr into the GB, the sample was annealed at 950^{o}c for 1 hour. During the annealing process, the Cu-Zr alloy experiences very little grain growth because of the reduction in GB energy with Zr segregation. The high-temperature annealing treatment is useful for the formation of AIF. To ensure the segregation lead into the formation of AIF; the sample was quickly quenched from 950^{o}c to room temperature.

The figure has been removed due to copyright issues

Figure 2-12: (a) AIF with thickness of 5.7 nm was observed at the GB after quenching; (b) GB in a slowly cooled sample.

From Figure 2-12(a), we can see the formation of AIF in the quenched Cu-Zr sample as the AIF region is quite disoredered from the crystalline part. In contrast, a similar Cu-Zr sample shown in figure 2-12 (b), which was slowly cooled after annealing at the same high-temperature does not show the formation of AIF. Crystalline order can still be observed all the way upto the GB. Although the GB in the sample from Figure 2-12 (b) were heavily segregated with Zr, the lack of AIFs proves that the amorphous structure shown in Figure 2-12 (a) is only in equilibrium at high temperature, in line with the thermodynamics of disordered GB complexion.

2.3.5. Effect of AIF in the deformation mechanism of NC metals

Previous studies have shown that a single dislocation can be absorbed by adding a specific burgers vector and slip plane in the grain. [63], [66], [67] But in the real case, nucleation and propagation of multiple dislocations occur concurrently and thus leading to the damage of the material. A first study to understand the effect of the presence of AIF was done by Z. Pan et al.

[15]. For a simple bi-crystal sample of Cu with the AIF from doped Zr, it was shown in the Figure 2-13 (a) and (b); the unambiguous evidence of having the effect of the AIF.

The figure has been removed due to copyright issues

Figure 2-13: Distribution of shear strain in (a) clean GB and (b) 1 nm thick AIF. [15]

The figure has been removed due to copyright issues

Figure 2-14: Distribution of shear strain at 5.7 nm thick AIF at a shear strain of (a) 2%, (b) 4.5%, (c) 6% and (d) 10% with a shear strain rate of 10^8 s^{-1}. [15]

From the Figure 2-14, we can see, with the increment of AIF thickness, high strain can be accumulated without initiating any crack. Finally, this study proposes that the strain concentrations are accommodated at the AIF by creating a vortex flow around the interface-dislocation intersection. And this vortex flow increases with the increment of absorbed dislocations till it reaches the other side of the AIF. Presence of the AIF delay the crack nucleation by spreading the stress concentration and even after nucleation of the crack, it can suppress the growth.

2.3.6. Effect of AIF in the strength of the material

There have been a few research on the effect of the complexion on the strength of the material. [19],[68] One of them could conclude the effect of having this complexion or AIFs over ordered interfaces.[19] By comparing three different micropillars; one with pure Cu ordered interface, the second one with segregated Cu-Zr ordered interfaces, and the third one being Cu-Zr with AIF. After the bending test, we can see that strain-to-failure value is the highest for the specimen with Cu-Zr AIF. For the other two cases, strain-to-failure values are much lower. Moreover, the micropillar with the Cu-Zr AIF shows the highest strength too. Figure 2-15 shows the differences

in the mechanical test on the three different NC Cu samples. It is clear that Cu-Zr with AIF exhibits the highest strain before failure during the bending test. Moreover, the yield stress of this sample is higher compared to the other two.

The figure has been removed due to copyright issues

Figure 2-15: Mechanical testing result from NC Cu and Cu-Zr; (a) pure Cu with ordered interfaces; (d) Cu-Zr with ordered interfaces; (g) Cu-Zr with AIF. (b) to (i) bending test result of the micropillars.[19]

From Figure 2-16, we can see the concluded data for the effect of AIFs in the strength of the material. The grey region shows the previous research data on strain-to-failure for Cu and Cu based alloy. We can see most of the data for Cu and Cu based alloy have a trade-off between strength and ductility.

The figure has been removed due to copyright issues

Figure 2-16: Direct comparison of the result between Rupert et al. with all previous studies based on the ductility of Cu and Cu based alloys. [19]

Therefore, by combining both nanostructuring and AIFs, it is possible to achieve both strength and ductility which overcomes the long conventional drawback of the NC materials.

A further study by the same research group has been performed recently to investigate the effect of AIFs in the increment of the strength of the material. [69] In this work, the researchers have investigated the influence of both ordered and disordered complexions in the plastic deformation mechanism of NC materials. Both complexions are characterized by their excess free

volume, and they promote dislocation emission by reducing the critical emission stress. On the other hand, the complexions act as strong pinning regions, and so, they increase the flow stress required to propagate the dislocations. These pinning regions are caused by ledges and solute atoms at the GB-complexion region. Therefore, they suggested that dislocation propagation is the rate-limiting mechanism behind the plasticity in NC materials and thus, influence the strength. [69]

The key observations in the previous experimental and simulation studies was to combine separate techniques of nanostructuring and GB complexion engineering into an effective way to use AIF effectively in lieu of regular GB. Furthermore, the introduction of NC materials with AIF will open a new class of material and broaden the suite of material properties that can be obtained. However, still some investigations are required to be done. Specifically, is there any size effect of the AIF in the NC metals? Does the deformation mechanism change with the presence of the AIF in the NC metals? In this thesis, we would to try find these answers with the help of numerical studies.

CHAPTER 3 Methodology

3.1. MD method

The main algorithm used in our research is the MD method. [70] It is a computational method that uses the classical law of mechanics to calculate the time-dependent behavior of molecules. Like other computational methods, the main goal of MD is to extend our understanding of experimental methods. However, in MD simulations, Newton's second law of motions are solved numerically along with the evolution of time to understand the kinetic and thermodynamic properties of a system. It is to be mentioned that, MD is very similar to real experiments, in which the statistical properties are measured for a given system or predicting the average behavior of a system under one or more known properties. The steps followed in an MD simulation are shown below:

1. Preparing the sample: At the very beginning, a model needs to be created that contains a specific number of atoms with specific properties like energy, temperature, volume, etc. Then this system needs to be initialized by assigning them temperature and initial velocities.
2. Simulation of the model: Next step is performing the simulation based on the parameters declared beforehand. In MD, Newton’s equations of motions are solved for the whole model, and thus, the positions of the atoms are updated accordingly.
3. Characterizing properties: Finally, from the updated positions, the required properties like temperature, volume, energy can be recorded and extracted.

3.1.1. Advantages of MD

Computer simulations help to get a better understanding of the structure and properties of a material. They also serve as complements to conventional experiments. There are many types of simulations, and among them, MD and Monte Carlo (MC) have upper hands on others due to their long-range techniques. For our research, we have used MD simulation because of the facts that MD gives way more dynamical properties of the entire system: time-dependent responses to perturbations, transport coefficients, rheological properties, and spectra.

Computer simulations act as a link between microscopic length and time scales with the macroscopic regime. At first, an assumption is provided at the interactions between molecules and exact predictions are achieved of the bulk properties of the material. These predictions can be made exact by controlling other parameters of the materials. At the same time, more information about the bulk material can be obtained through this simulation. However, these simulations act as a link between experiments in another way too: which is between theory and experiment. These simulations can test any theory and model and compare the results with experiments. Another advantage is that simulations can be carried out in extreme environment parameters such as, elevated temperature and pressure, which might be difficult to obtain in experiments at some points.

Figure 3-1 Bridge between simulation and experiments[70]

Figure 3-1 shows the link between experiments and simulations, and how simulations can solve complex practical problems to obtain a solution. Finally, among the other simulation methods, MD aims to get rid of the redundant parts of the experiments and provide comparable

results between experiments and modeling.

3.1.2. Molecular dynamics algorithm

In MD simulations, these are the general steps that are being followed: [71]

a. Building the model: The geometry, structure, types of atoms and molecules along with the interparticle potential are declared in this step.
b. Initializing the model: In the beginning, the constructed model is not considered as a physical one, as there is no force between the atoms only because of the reason that initial temperature is 0 K. Therefore, the temperature must be assigned to achieve an equilibrium model.
c. Assigning temperature: The statistical mechanics is used to assign the temperature in such a way so that, the whole model obtains the desired temperature following the Gaussian distribution.

3.1.3. Periodic boundary condition (PBC)

Generally, while simulating a molecular system, the number of particles of the whole system should be in the order of magnitude of the Avogadro number (~10^{23} atoms). However, one of the limitations of MD is that the number of atoms we can simulate (~10^{6} atoms) is far-fetched compared to the ideal scenario. Implementation of PBC can alleviate this problem by considering an infinite array of identical copies of the whole simulation box. [72]

3.1.4. Thermodynamic ensembles

In statistical mechanics, to represent the possible states of a mechanical system in thermal equilibrium with respect to a heat bath at a fixed temperature, special types of ensembles are used. As the system exchange energy with the heat bath, the state of the system will differ in total energy as well. The most common ensembles used in MD are shown below:

a. Canonical ensemble (NVT): In this system, the distribution of the state is determined by keeping the temperature absolute. This ensemble depends on mechanical variables such as the number of particles in the system (N) and the system's volume (V). This is also known as NVT ensemble. Therefore, this system keeps the temperature with an average threshold value by allowing the total energy to fluctuate.
b. Isothermal-isobaric ensemble (NPT): This one is a statistical mechanical ensemble by keeping the temperature (T), constant pressure (P) constant along with the number of particles (N). This system maintains an average value of pressure while fluctuating the volume of the system.
c. Microcanonical ensemble (NVE): This ensemble system is isolated from the changes in a number of atoms (N), volume (V) and energy (E). There is no heat exchange is this system. There is an exchange between potential and kinetic energy by keeping the total energy conserved.

3.1.5. Embedded atomic method (EAM) potential

The EAM potential is an approximation describing the energy between atoms as a function of a sum of functions of the separation between an atom and its neighbors. It is one of the most used potentials or metallic materials. Force-field for EAM is obtained from more accurate methods such as ab initio or semi-empirical methods.[73] In a simulation, the potential energy of an atom, i, is given by

$$E_i = F_\alpha \left(\Sigma_{i \neq j} \rho\beta(r_{ij}) \right) + \frac{1}{2} \Sigma_{i \neq j} \varphi_{\alpha\beta}(r_{ij}) \qquad 1$$

where rij is the distance between atoms i and j, $\varphi\alpha\beta$ is a pair-wise potential function, $\rho\beta$ is the contribution to the electron charge density from atom j of type β at the location of atom i, and F is an embedding function that represents the energy required to place atom i of type α into the

electron cloud. We have used the EAM for copper (Cu)[74] [75] and copper-zirconium (CuZr)[76] for this research work.

3.1. Software

3.1.1. Large-scale atomic/molecular massively parallel simulator (LAMMPS)

In my research, all the simulations were performed using LAMMPS [71] which met our requirement for the force field. LAMMPS is an MD program from Sandia National Laboratories which can work together with Python. For computational efficiency, LAMMPS uses neighbor lists to keep track of nearby particles. The lists are optimized for systems with particles that are repulsive at short distances so that the local density of particles never becomes too large. On parallel computers, LAMMPS uses spatial- decomposition techniques to partition the simulation domain into small 3d sub-domains, one of which is assigned to each processor. Processors communicate and store "ghost" atom information for atoms that border their sub-domain. LAMMPS is most efficient (in a parallel computing sense) for systems whose particles fill a 3D rectangular box with approximately uniform density.

3.1.2. Ovito

Ovito [76] was used for the visualization and image generation of all atomistic configurations in my study. It is free atomistic visualization software for all major UNIX platforms. It can handle more than one million atoms on a PC with 1 GB memory. It is a robust, low-cost tool for surveying nanostructures and following their evolutions. In my study, all the result images are generated from Ovito.

3.2. Models used in this thesis

We have used three different models for the whole work. At first, we have used a Cu bi-crystal with AIF shown in Figure 3-2(b). For the simulation and analysis purpose, we have changed the single crystalline interface orientation to different ranges.

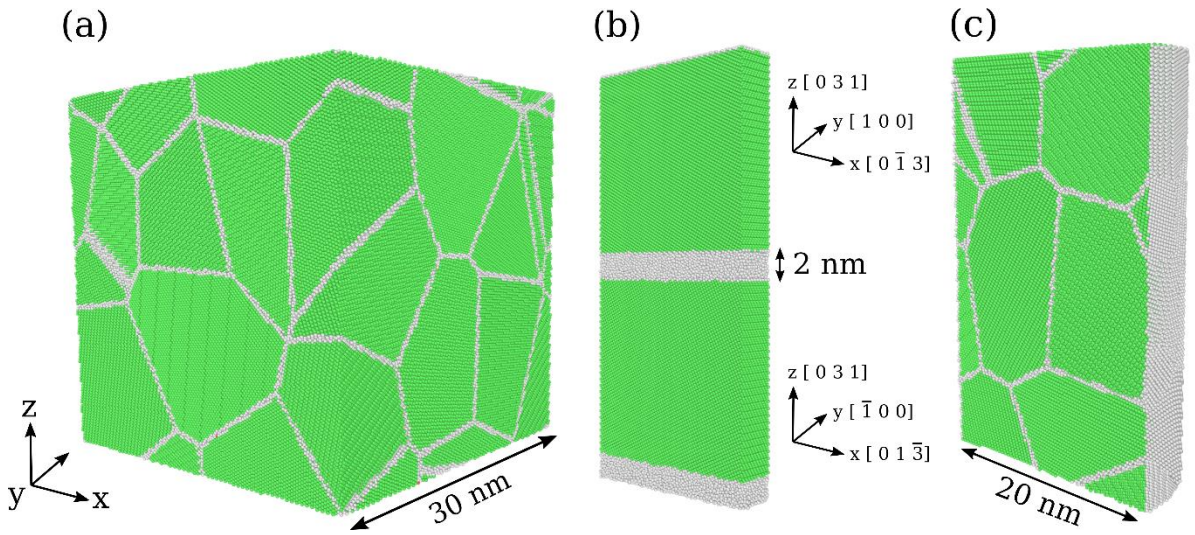

Figure 3-2 : (a) Atomistic configuration of pure NC Cu model with a grain size of 9 nm. This model contains approximately 2 million atoms. The dimension of the model is 30 x 30 x 30 nm. (b) Bi-crystal Cu model with the AIF of 2 nm. Orientations for the upper and lower crystals are indicated on the side of the bi-crystal. (c) NW Cu with a diameter of 20 nm and grain size of 11 nm. This specific model contains the AIF of 1.0 nm. Here, according to common neighbour analysis, green colored atoms stand for face-centered cubic structure and white colored atoms stand for unknown coordination structure.

Most of the used models in our research are shown in Figure 3-2(a). For the pure NC Cu models, we have varied the grain sizes from a smaller size of 3 nm to as high as 17 nm. We have artificially changed the infrastructure of the Pure NC Cu with the CuZr AIFs and varied the AIF

thicknesses from 0.5 nm to 1.5 nm. Finally, we have used another model made from our 3D NC Cu model which is a nanowire (NW) with a grain diameter of 20 nm.

3.2.1. Amorphous CuZr model

It is important to mention that, for all through our work, we have used the same CuZr AIF. The composition of this film was 64% of Cu and 36%. of Zr. There are a few reasons for choosing Cu and Zr as our amorphous model. The most important reason is that it is possible to synthesize this amorphous material in practice because of their large atomic size mismatch. [77]Again Zr has a high tendency to segregate to the GB of Cu. [78]These two metals have shown good glass forming ability as well. [79] Finally, one last key reason is large simulation data is available for the CuZr based amorphous materials. [80]–[82] For making this model, we first built a thin slab of a crystalline model of Cu. Then we replaced 36% atoms of Cu with Zr. Being consistent with the literature, we have heated the model applying Nosé and Hoover thermostat method at 2000 K for 150 ps. After the heating and holding period, the model was cooled down to 10 K in three steps. Firstly, it was cooled down to 1000 K in a rapid cooling rate step (4 K/ps). In the second step, we have cooled down the model until the glass transition temperature of 700^{o} Celsius in a slow cooling rate (0.12 K/ps) to ensure that amorphization occurs. [83], [84] Finally, we have quenched the whole model from 700K to 10 K using a quenching rate of 1.38 K/ps and relaxed by using Nosé and Hoover thermostat at the same temperature.

Lastly, we have performed a radial distribution function (RDF) analysis [85] to confirm the validity of our model. It is already established that amorphous materials show a long-range order instead of short-range of crystalline materials. From Figure 3-3, we can see only one sharp peak the beginning followed by two or three small peaks before the curve reaches a plateau. [86], [87]

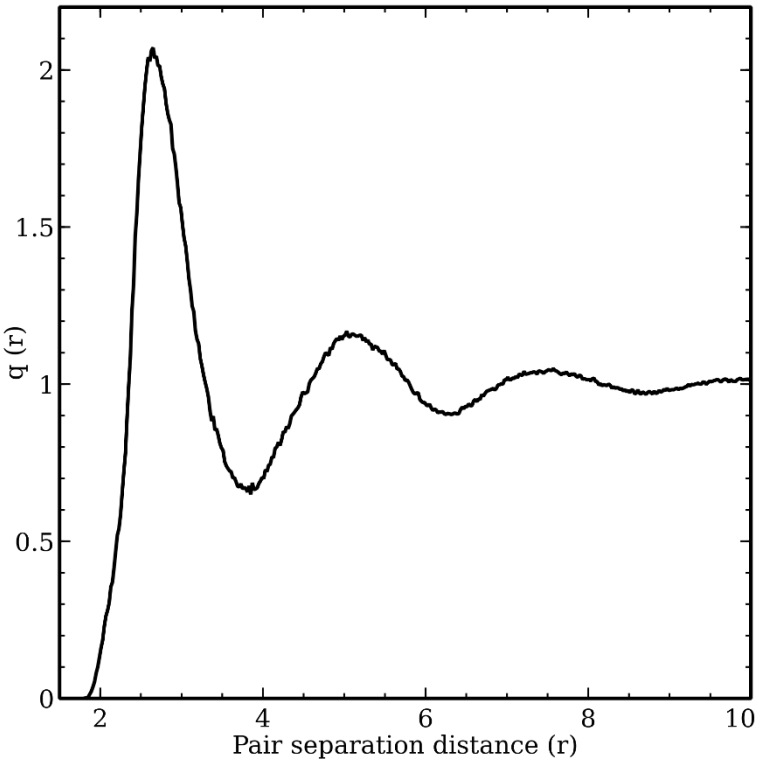

Figure 3-3: RDF analysis of the amorphous CuZr sample

3.2.2. NC Cu models

For making the 3D NC Cu models, we have used a software named Atomsk. [88] All our 3D NC Cu models have the same dimension of 30 nm in every direction, *i.e.*, x, y, z directions. At first, we need to generate a LAMMPS file which contains the unit cell data for Cu by using xtal. [88] Then, we need to input the data such as dimensions, number of grains to obtain our desired models. For varying the grain sizes, we have controlled the total number of grains in the models. Since the dimension of the model is fixed, by changing the number of grains, we can control the grain size and thus, vary the grain sizes from 3 nm to 17 nm. In Figure 3-2 (a), we can see a pure 3D NC Cu model with a grain size of 9 nm which has been made by this process.

3.2.3. NC Cu models with AIF

To build our NC Cu models with AIF, at first, we had to make sure all the models mentioned above have been relaxed to the same temperature. For our simulation set, we have always used 100 K as the final relaxation temperature. Using Ovito, we can remove any type of atoms from the models. Since Ovito uses a special color code for the visualization of the atoms, we could easily remove all the atoms from the GB region of the NC Cu models. After that, we have made an amorphous CuZr model with the exact dimensions from NC Cu models. Using LAMMPS, we can join both models together and remove the amorphous CuZr atoms from the grain interiors only. In that way, we would be left with only pure Cu inside the grains and amorphous CuZr at the GB region. To validate our model, we again performed a heating and quenching process. We have heated the model to 900 K for 150 ps. After the holding period, we have quenched it to 100 K with a quenching rate of 0.4 K/ps relaxed by using Nosé and Hoover thermostat at the same temperature. Thus, we have obtained 3D NC Cu models with AIF.

3.3. Simulation parameters

We have used two types of temperature in the whole set of simulation; 100 K and 800 K. At first, to bring the models to the desired temperature, an isobaric thermostat developed by Nosé and Hoover [89] for $100\ ns$ was applied to the models. During the simulation to keep the model at the temperature, canonical NVT thermostat was used. [90] The time step used in this work was $5\ fs$. Ovito was used to visualize the atomistic configurations and to determine the different crystallographic systems (such as FCC, HPC or stacking faults) Common Neighbour Atom (CNA) [91] method was used. To compute the atomic stresses Virial theorem [71] was applied as follow,

$$\tau_{ij} = \frac{1}{\Omega}\sum_{k\in\Omega}\left(-m^{(k)}\left(u_i^{(k)} - \bar{u}_i\right)\left(u_j^{(k)} - \bar{u}_j\right) + \frac{1}{2}\sum_{l\in\Omega}\left(x_i^{(l)} - x_i^{(k)}\right)f_j^{(kl)}\right) \qquad 2$$

in which k and l are atoms, Ω is the volume of the domain, $m^{(k)}$ is the mass of atom k, $u_i^{(k)}$is the i^{th} component of the velocity vector of atom k, $\bar{u}_j$ is the j^{th} component of the average velocity of atoms in the volume, $x_i^{(k)}$ is the i^{th} component of the position of atom k and $f_j^{(kl)}$ is the j^{th} component of the force applied on atom k by atom l.

Two different loading was used in this research work to apply deformation. Firstly, to apply shear two thin slabs of atoms were defined as rigid bodies at the top and bottom of the model. The lower was fixed, and the top was moved in the direction parallel to the GB plane to apply shear on the GB. Secondly, for tension, we have applied the constant engineering strain rate. This style changes a dimension of the box at the units of the specified strain rate. We have applied a constant strain rate of 10^8/s in the z-direction for 15 ns.

We have used atomic strain modifier from Ovito to analyze our models under tensile loading. This modifier calculates the atomic-level strain tensors based on two configurations of the system. [92], [93] The data set to which the modifier is applied is considered the current configuration of the system. And there is reference configuration of the system which is loaded from a separate input file by the modifier. OVITO calculates the local deformation gradient tensor F for each particle from the relative displacements of the particle's neighbors within the given cut-off radius. It is important that the reference file must contain the same number of particles as the deformed configuration received by the modifier. To calculate the displacement of a given particle in the deformed configuration, the modifier needs to find the corresponding particle in the reference

configuration of the system. If particles possess unique IDs, the modifier will use this information to map particles from the reference configuration to the current configuration and vice versa. If no particle IDs are defined, the modifier assumes that particles have the same ordering in both configurations. Finally, another modifier named color coding is used to map the deformation in the models. This modifier assigns colors to particles based on one of their properties like potential energy, shear strain, etc. It thus provides a simple method to visualize scalar per-particle quantities.

CHAPTER 4 Results and discussion

We have divided this chapter into three sections. The first section discusses the effect of interface orientation of bi-crystalline Cu with the AIF on the interfacial energy and shear strength. The second section is about the influence of the AIF in a NC Cu when tensile loading is being applied. We also discuss the deformation mechanism at lower and higher temperature in this section. The third section discusses the toughness test of our material by comparing our result with the previous literature works.

4.1. Influence of the AIF in bi-crystal Cu

4.1.1. Effect of AIFs in interface energy

We have performed simulations on our pure bi-crystal Cu at first for determining the interface energy at the beginning. Results for interface energy for the pure Cu bi-crystals have already been investigated and published by various researchers, and it has been found that interface energy mostly depends on the orientation of the interface. It has been found that based on misorientations, these interface energy values can widely vary from a small value of 0.1 J/m^2 to almost 1.5 J/m^2. [66], [94]–[98] As we wanted to validate our pure bi-crystal Cu models, we have performed the same simulations at 100 K. In the results of our simulations, we have found our values for different orientation from 0.1 J/m^2 to 1.24 J/m^2 which is shown in Figure 4-1. These values agree with all the previous data published in literature. It is important to mention that we have chosen these orientations randomly and we have a very special orientation in our dataset which is (111). [99], [100] As we can see, only for this orientation interface energy value is the least of them because this misorientation angle forms a particular type of boundary which is known as the twin boundary. [82], [83] To investigate the effect of amorphous GB in our same bi-crystal models, we have replaced our regular GB atoms with AIFs shown in Figure 4-1.

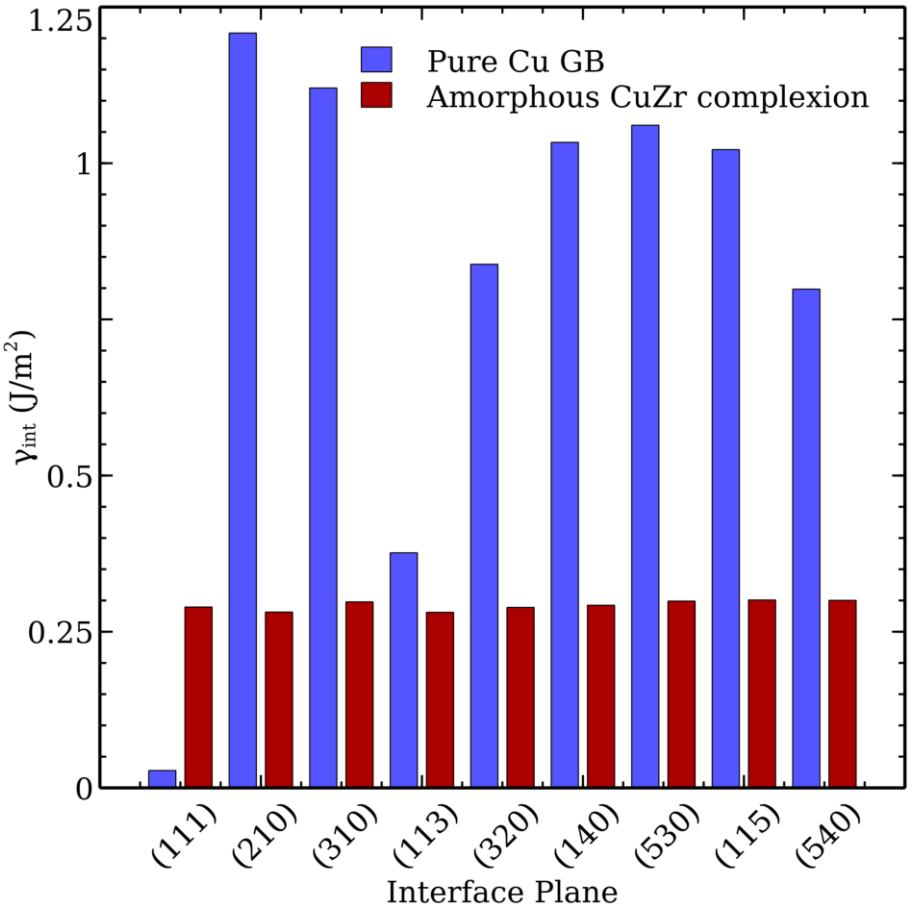

Figure 4-1: Effect of (a) Pure Cu GB and (b) AIFs in the Cu bi-crystal models. Orientations of the planes and energy values are shown in the x and y-axes respectively.

After that, we have applied the same conditions and temperatures for these models and performed the simulation. To obtain the interface energy, we have used the following equation:

$$\gamma_{int} = (\gamma_{total} - \gamma_{crystal} - \gamma_{amorphous})/S_{int} \qquad 3$$

In this equation, γ_{total} is the summation of potential energy in a well-relaxed bi-crystal Cu with AIF model for all atoms and will be referred to as the total energy in this current study. The terms

γ_{crystal} and $\gamma_{\text{amorphous}}$ are the total energy of the crystalline and AIF layers before joining together, respectively. S_{int} represents the cross-sectional area of the interface.

The results we have got from these simulations are also shown in the Figure 4-1. It is found that while using the AIFs, the interface energy values largely change from its pure interface models, and now all these interface energy values fall in a closed regime which is approximately from 0.275 J/m^2 to 0.295 J/m^2. This result opens a new perspective regarding the effect of the AIF in the interface energy of bi-crystals as well as NC models. Also, from our results, the most important part we can claim that, by introducing the AIF, these energy values no longer depend on the misorientation angle. Instead, they make all the models relatively homogenous in terms of energy. Moreover, as we know from the Gibbs free energy, all the atoms tend to reduce their energy to achieve stability, we can certainly say that these AIFs have not only made the energy values fall in a close range but also reduced the values by a significant margin.

4.1.2. Effect of the AIFs under shear loading

We have performed the shear deformation process on the bi-crystal Cu with the AIF at 100 K in this process. It has been discussed already how we have applied the shear on these models in chapter 3. For this set of simulations, we have chosen only bi-crystals with the AIF because deformation mechanism on pure bi-crystal Cu has already been discussed in previous literature. [103]–[106] For the AIF, we have selected the width as 0.5 nm, 1.0 nm, 2.0 nm and 5.0 nm to understand not only the effect of the AIFs but also, if there is any size effect of the widths of AIFs. From Figure 4-2 (a) we can see the shear stress vs. time curve. When the AIF width is 0.5 nm, we can see sharp peaks. These peaks are similar to the ones when shear is applied on pure bi-crystal Cu. But these peaks reduce as the GB width is increased gradually. And, we see less sharp and convoluted peaks instead of the previous one. To do more analysis, we have performed atomic

strain analysis on these models using Ovito, and we can see the analysis Figures from 4-2 (b) to (e).

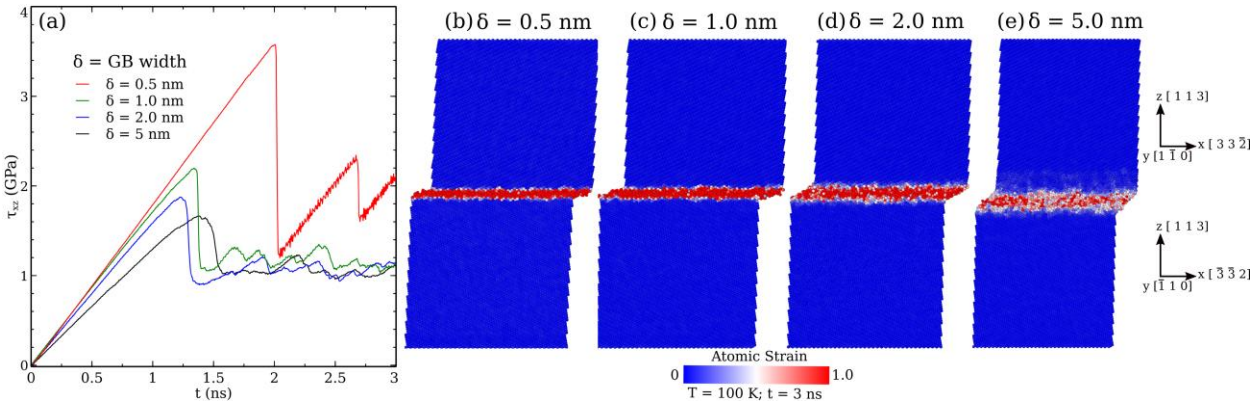

Figure 4-2 – (a) Shear stress-time curve of bi-crystal Cu with AIF varying the AIF width from 0.5 nm to 5 nm; (b) – (e) Atomic strain analysis for the bi-crystal Cu model with the interface orientation of (113) shown on the right side.

When the AIF thickness is 0.5 nm, after 3 ns of deformation, the interface is already under high strain, and due to the deformation process, we can see the upper crystalline part sliding with respect to the lower crystalline part. For 0.5 nm, the atomic fraction for the AIF potion is too low, and still, this bi-crystal is behaving like a pure bi-crystal Cu. That is why we can see pure sliding instead of shear when then the AIF width is 0.5 nm. However, with the increment of the AIF width, atoms at the interface seem to under less strain as they seem to appear as a mixture of red and white atoms. Although AIF width 1.0 nm and 2.0 nm are still showing partial sliding, we can see a different deformation process for 5.0 nm AIF width. Here, the atoms at the interface are not under much strain (referring to the color map) compared to the other models. And, we do not see any sliding process under deformation for this model too. Because of the presence of the AIF, the

deformation process starts with the amorphous atoms only which finally will shift to the interface with given time. Therefore, we can say, by increasing the AIF widths, we can find a different deformation process compared to the convention pure bi-crystals under shear loading.

4.2. Effect of the AIF under tensile loading at low temperature (100 K)

4.2.1. Effect of tensile loading on pure Cu interface

In this part, we will discuss the effect of having the AIF in a NC material at a low temperature of 100 K. In this part of our simulations, to avoid the effect of thermal fluctuation, we have chosen 100 K as our fixed temperature. In the beginning, we have applied tensile loading on the pure NC Cu models. The method of applying tensile loading has been discussed in chapter 3. For this part of the simulation, we wanted to investigate the effect of grain sizes of the models. Therefore, we have varied the models from a relatively smaller grain size of 3 nm to higher grain sizes of 5 nm, 7 nm, 9 nm, 11 nm, 15 nm and 17 nm. The results for this simulation have been exhibited at Figure 4-3 (a). As we can see from this part of the figure, while applying tensile loading on these grain sizes, from a grain size of 3 nm to 15 nm, there has been an increase in the stress value; specially if we consider the peak stress values, we can look up in the region and say that these values are changing from 1.5 GPa to almost 1.8 GPa.

However, when we move to the grain size of 17 nm, we can certainly see a drop at the whole stress level. This phenomenon has already been established and explained by several researchers, famously known as IHPE. As we have discussed in the literature review, while applying to load on a NC model, it is very much possible to see this kind drop in the stress level while we are increasing the grain size from a smaller value to a larger one. Moreover, the values we have got from the simulation, they do agree with previous data both from experiments and on a NC model, it is very much possible to see this kind drop in the stress level while we are increasing the grain

size from a smaller value to a larger one.

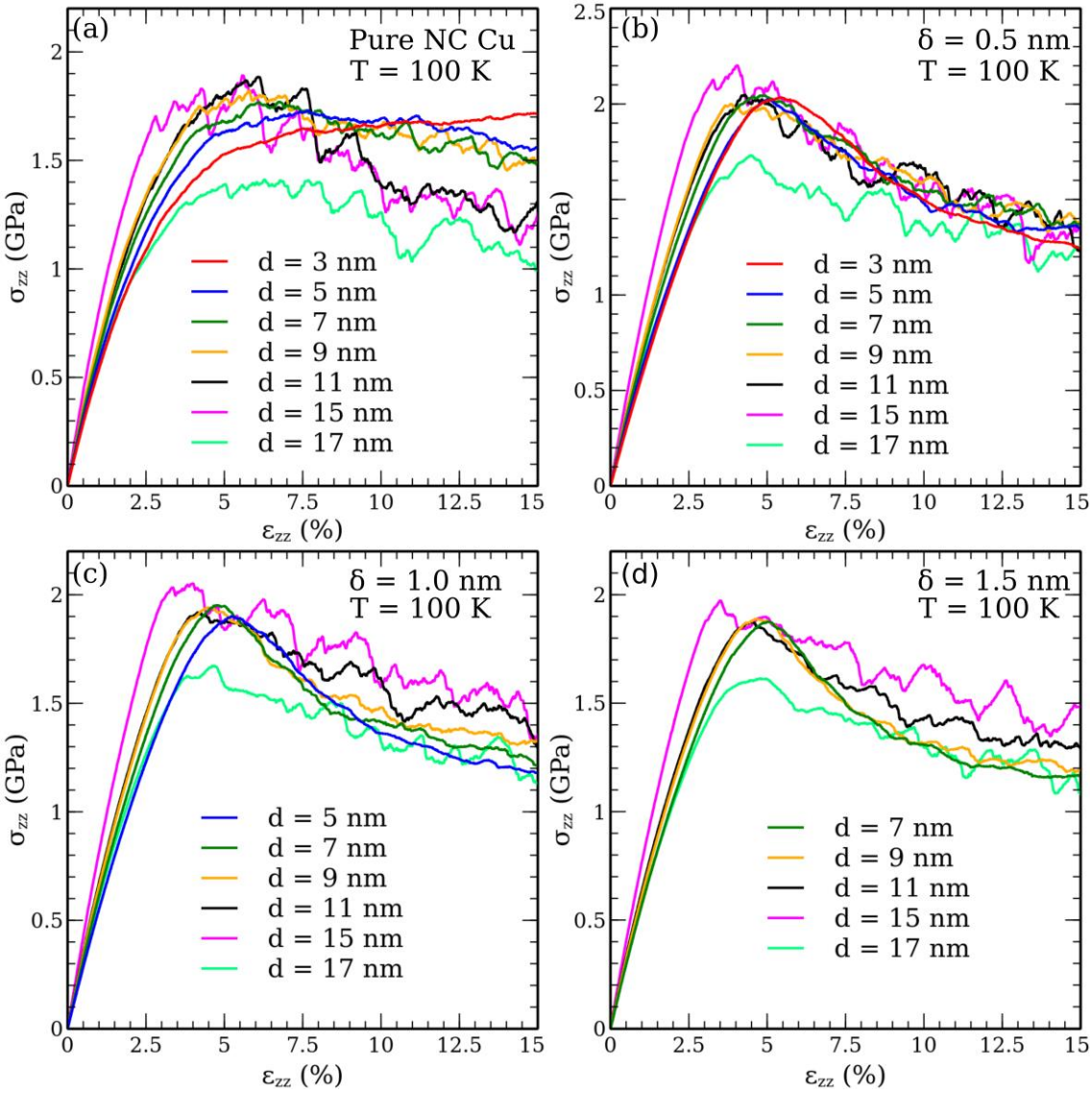

Figure 4-3: Stress-strain curve of NC Cu at 100 K varying grain sizes from 3 nm to 17 nm with (a) pure Cu GB; (b) AIF with 0.5 nm thickness; (c) AIF with 1.0 nm thickness and (d) AIF with 1.5 nm thickness.

Moreover, the values we have got from the simulation, they do agree with previous data both from experiments and we can see a trend of strong strain hardening for this grain size which

is not typical for all other grain sizes. Instead, we do see a lot of ups and downs in the peaks which stand for dislocations. The reason is due to smaller grain sizes in the NC model; it might be possible that we do not see many dislocations nucleating and propagating through the grains due to the lower temperature. However, with the increment of the grain sizes, we do see more activity of dislocations.

4.2.2. Effect of tensile loading on the AIF

In this part, the same approach of tensile loading has been applied to the NC models with the AIF. Again, we have varied the grain sizes from a smaller value of 3 nm to 17 nm to investigate the grain size effect. Moreover, we have varied our AIF thickness as well in this part to see if the thicknesses of AIFs have any effects under the tensile loading. From Figure 4-3(b), we can see the stress-strain curve for NC Cu with an AIF thickness of 0.5 nm. We have kept the AIF thickness fixed and varied the grain diameter from 3 nm to 17 nm like previously and thus applied the same strain rate (10^8/s) for all the simulation models. However, we could not include all the grain sizes such as 3 nm and 5 nm when we changed the AIF thickness to 1.0 nm and 1.5 nm. When we increase the AIF thickness in those very small grain sizes, the percentage of the amorphous atoms increases to a very high level turning the whole model as a different composite. Therefore, if we apply the tensile loading, we would only find the deformation mechanism of the AIF only. As we can see from the trends in the curve of Figure 4-3(b), the first thing that has changed in this part compared to the pure interfaces is the value of stress level. While the range for the stress value was around 1.4 GPa to 1.9 Gpa for the previous case, here we can see an increment in the stress value from 1.65 GPa to 2.3 GPa approximately. Moreover, we do see that there have been fewer dislocations when the grain size is smaller, but with the increment in grain size, we do find higher dislocations. The same type of parameters has been applied to our next

set of simulations when we have changed the AIF thickness from 0.5 nm to 1.0 nm and 1.5 nm. We can see the stress-strain curves for these AIFs thicknesses in Figure 4-3 (c) and (d) respectively. Again, for both thicknesses, we do see an increment in the stress level. Most importantly, we can see the shift in the yield stress value from 15 nm to 17 nm of grain diameter with all these three AIFs thicknesses. It means even if we changed our interfaces to AIFs thicknesses, we have achieved a higher stress level, but our models still agree with the conventional IHPE. More scrutinized effect of grain diameters and AIFs thicknesses will be discussed in the next section.

4.2.3. Effect of grain sizes and AIFs thicknesses under tensile loading (flow stress)

As we have discussed the stress-strain curves in our previous section, now we will investigate the effect of having various grain diameter along with the change in the AIFs thicknesses with respect to flow stress.

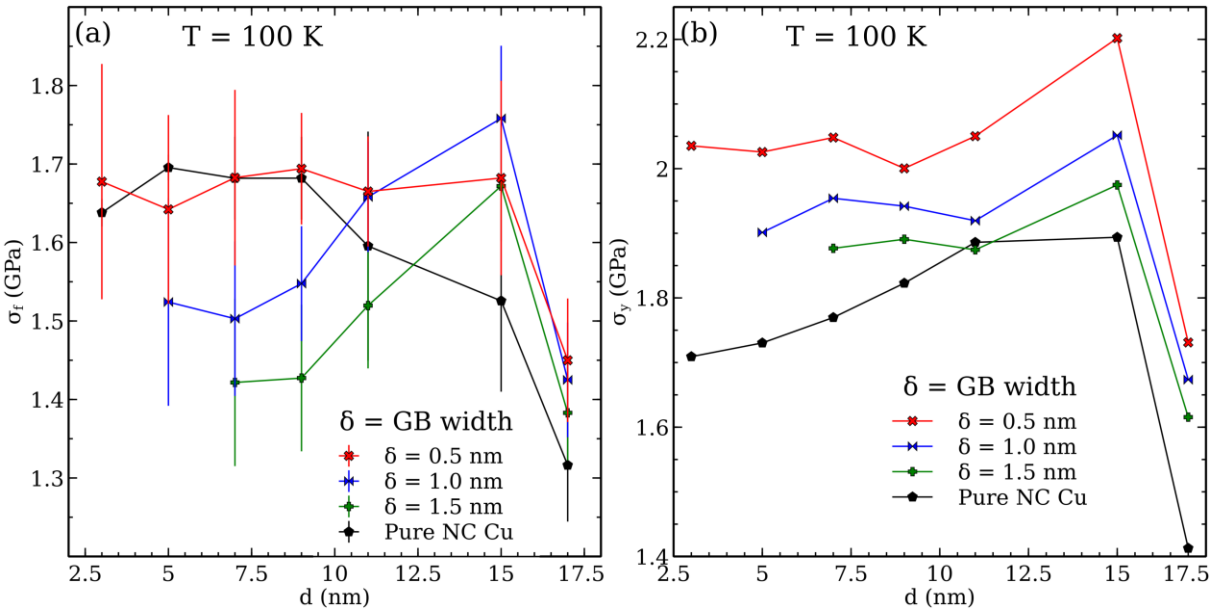

Figure 4-4: (a) Flow stress vs. gain diameter curve showing grain sizes from 3 nm to 17 nm with AIF thickness from 0.5 nm to 1.5 nm including pure NC Cu at 100 K; (b) yield stress vs. grain diameter graph with the same parameters at 100 K.

In previous literature, researchers have used the term of flow stress with various strain values. However, in general, most of them have agreed upon the same definition which is flow stress depicts the strain regime where the plastic deformation of a NC material occurs under any mechanical loading. [34], [107] For our cases, if we again look at Figure 4-3 (a-d), we do see that most of the part of the plastic deformation occurs under a strain of 5.5% to 10% mostly. Therefore, we have chosen this range for our flow stress region and thus, averaged the values that fall under this region to obtain the individual flow stress value for each grain diameter with three types of interface thicknesses. If we look at Figure 4-4, the black trend line exhibits the change in flow stress with the variation in grain diameter when the interface is pure Cu. As explained before, we do see the increment in the flow stress values as the grain diameter increases from 3 nm to 9 nm, and then there is a sharp drop from 15 nm to 17 nm. From this trendline, the IHPE phenomenon is way more visible. The other three trendlines exhibit the flow stress values for the three different AIFs thicknesses. When the AIF thickness is 0.5 nm, we see that for a grain diameter of 3 nm and 5 nm, flow stress value is shifting between this AIF thickness and pure Cu interface. With further increment in the grain diameter, we find the difference in the flow stress to a more significant margin. Moving to AIF thickness of 1.0 nm, we find a whole different scenario in this case. Till the grain diameter becomes 11 nm, NC models with pure Cu interface have higher flow stress values, but a significant shift occurs in 15 nm, and the sudden drops occur in 17 nm. Moreover, for the final case, we see a very similar trendline for the NC model with 1.5 nm AIF. Another thing we can highlight from these graphs that except for lower

grain sizes, *i.e.*, 5 nm or 7 nm, we see an overall increment in strength for all AIFs thicknesses. In practical, it is relatively easier to synthesize a material with a dimension of tens. Therefore, it will be easier to synthesize a NC Cu material with AIFs that exhibit higher strength. Considering all the facts, we can finally state that, by introducing AIFs in the NC materials, it is possible to achieve a higher flow stress. For an optimum size of grain diameter and AIFs, it is possible to obtain a stronger NC material compared to its pure interface thickness materials.

4.2.4. Effect of grain sizes and AIFs thicknesses under tensile loading (Yield stress)

Moving onto the next part, now we are comparing between the yield stress values between the pure NC Cu material with the NC Cu with three different AIFs thicknesses shown in Figure 4-4 (b). By considering the yield stress, we can directly compare between their deformation initiation time. From the simulation data set, we have chosen 0.2% offset of the stress values to find the yield stress and thus, plotted the graph. For pure NC Cu, we can see a steady increment in the yield stress value from 3 nm to 11 nm, retaining this value and then a sharp drop from 15 nm to 17 nm. Like all our previous results, this trendline agrees with other published value in the literature. [34], [107], [108] However, we do have a completely different trend when it comes to AIF thickness of 0.5 nm. For the smaller grain sizes, there is an up and down in the yield stress values up to 9 nm, but after that, there is a sharp increment from 2.05 GPa to 2.22 GPa. If we compare the value between AIF thickness 0.5 nm to pure NC Cu model, there is a distinguishable difference in the yield stress value which is 1.9 GPa to 2.22 GPa due to typical solute segregation and strengthening. Although this yield stress value seems to drop slightly for the other two types of AIF, however, these values are still ahead compared to pure NC Cu by a clear margin. It is important to mention that for all the models, the IHPE increases from 15 nm to 17 nm has been consistent. Finally, from these results, we can again confirm that, for an optimum grain diameter

with AIF thickness, it is possible to obtain a NC Cu model with higher strength.

4.2.5. Effect of the AIFs under tensile loading at high-temperature (800 K)

To understand the impact of the AIF during high-temperature tensile loading, we have selected the same models and heated them up to a temperature of 800 K. For applying heat, we have followed the NPT method. After that, we have applied the same rate of strain (10^8/s) to all these models. Results are given in the following figure:

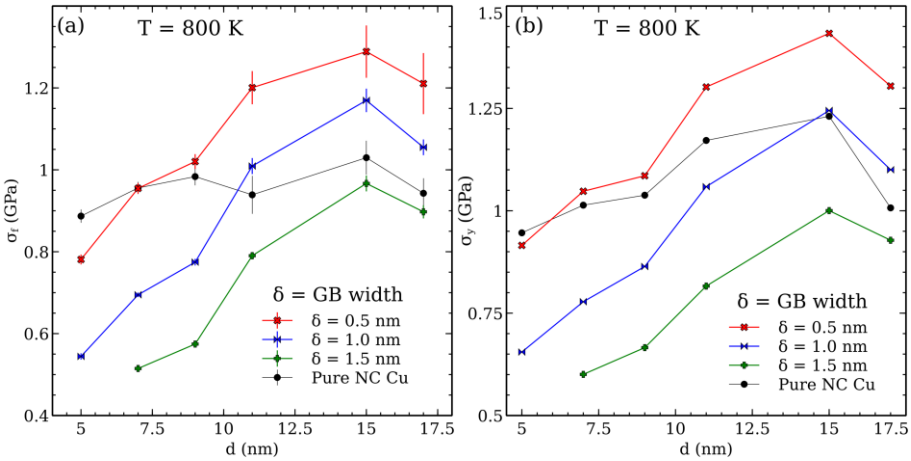

Figure 4-5: (a) Flow stress vs. gain diameter curve showing grain sizes from 3 nm to 17 nm with AIF thicknesses from 0.5 nm to 1.5 nm including pure NC Cu (black) at 800 K; (b) yield stress vs. grain diameter graph with the same parameters at 800 K.

The first findings we can get from both graphs; Figure 4-5 (a) and (b); we can find the IHPE relationships even at the high temperature. We can see the shift in stress (both flow and yield) from 15 nm to 17 nm. This shift in the stress matches with our previous simulation data. So, temperature does not have any impact on the IHPE relationship. However, if we look at the stress values, we do see different values compared to the data at 100 K. Here, in both cases, flow stresses and yield stresses have decreased. The main reason behind this phenomenon is the thermal effects of the

high-temperature; and so, the whole structure gets weaker. Furthermore, if we compare the values among the pure NC Cu to NC Cu with the AIFs, we do find that, models with AIF thickness of 0.5 nm and 1.0 nm exhibit higher strength in both cases. Although AIF 1.5 nm show less strength compared to all the other models. Since the amorphous material is originally from the metallic glass; the amorphous layer seems to be soft at the high-temperature specially if the temperature is close to or higher than its glass transition temperature. This is the main reason for not obtaining a higher strength when we have an AIF thickness of 1.5 nm.

4.2.6. Effect of the AIF in the deformation mechanism

We have seen that by substituting the AIFs instead of regular GBs, there has been a significant change in the flow stress as well as yield stress of the materials. To investigate the main reason for this effect, we have analyzed both changes in AIF thickness and grain size.

4.2.7. Effect while changing the AIF thickness

To understand the impact of the AIF, we have selected grain sizes of 17 nm out of our all models. One of the reasons for choosing this size is to understand the core deformation mechanism going right after the IHPE occurs. Along with this grain size for pure NC Cu, we have analyzed three AIFs thicknesses from 0.5 nm to 1.5 nm. For the analysis, we have implemented atomic strain analysis. From Figure 4-6(a), we see the pure NC Cu model after 15% strain at 100 K. The red bands shown in the images are exhibiting the GB regions and the white show the dislocations. At a high strain of 15%, we can see lots of dislocations nucleating and propagating through the grains which are expected from previous results. If we look at the Figure 4-3(a), for grain diameter of 17 nm, we do see lots of peaks which stand for these dislocations. After substituting this pure GB with the AIFs, we find different results. When the AIF thickness is 0.5 nm, the GB has not formed into AIF completely, rather it exhibits behavior

close to pure crystalline part. That is why we still see a sizable number of dislocations. But moving on the higher AIF thickness, we can see fewer dislocations. Especially, at the AIF thickness of 1.5 nm, the number of dislocations propagating through the grain sizes are the least. The same analysis has been done on models at 800 K, and we can see the result of the analysis from Figure 4-6(b).

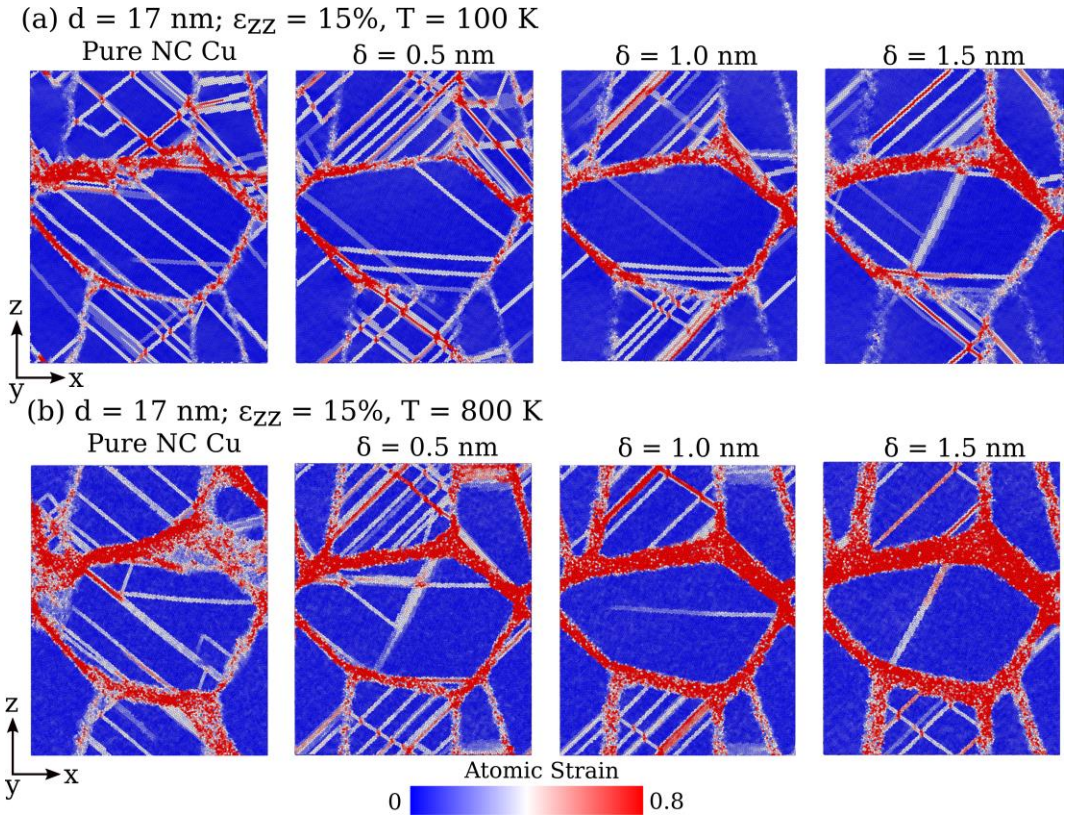

Figure 4-6 Atomic strain analysis for NC Cu with pure GB and AIFs thicknesses from 0.5 nm to 1.5 nm at (a) 100 K and (b) 800 K. The red atom bands depict for the GB areas whereas the white lines stand for the dislocations. All these images are at a strain of 15%.

The similar trend can be seen in Figure 4-6 (b). As the AIF thickness increases, fewer dislocations can be observed. At high temperature, GB activity act as the dominant mechanism over dislocation nucleation and propagation. That is why we can see more GB activity along with a few dislocations.

4.2.8. Effect while changing the grain size

To investigate the deformation mechanism of the NC Cu with the AIFs, we studied the effect of different grain sizes keeping the AIF thickness same for all of them, *i.e.*, 1.0 nm. From Figure 4-7 (a), we see the atomic strain analysis for the models at 100 K. After 15% strain, we see fewer dislocations propagating through the grain when the grain size is only 5 nm. As the grain size increases, it is expected to find more dislocation activities because of the volume fraction of atoms in the GB areas. And, we find the same GB activities in our models. When the grain size is smaller, more GB activity can be observed instead of dislocations due to the presence of a higher percentage of AIFs. With the increment of the grain sizes, we do see more dislocation activities. The same behavior can be seen when the temperature is 800 K. When the grain size is smaller, due to high-temperature, a high amount of GB activity can be observed from the Figure 4-7 (b).

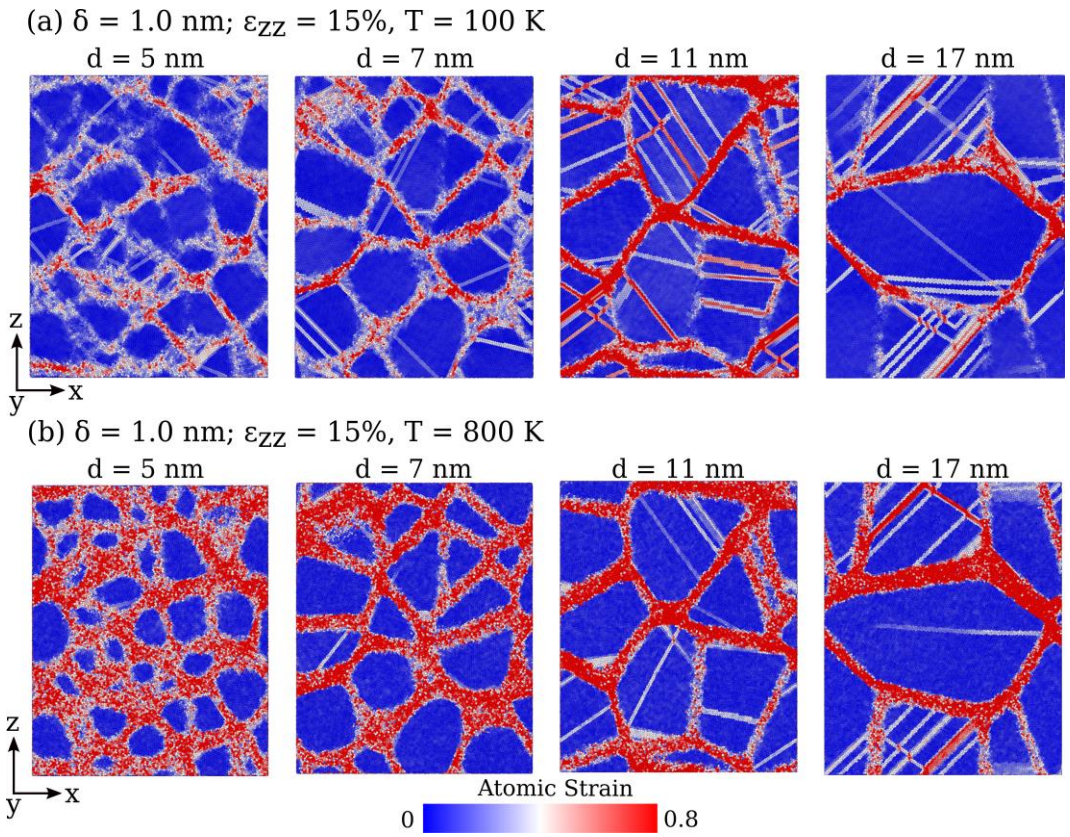

Figure 4-7 exhibits the atomic strain analysis for NC Cu varying grain sizes from 5 nm to 17 nm with the same AIF of 1.0 nm at (a) 100 K and (b) 800 K. The red atom bands depict for the GB areas whereas the white lines stand for the dislocations. All these images are at a strain of 15%.

However, with the increment of grain sizes, we see more dislocations. It is notable that, at 800 K, we see fewer dislocations even in higher grain sizes compared to 100 K. As GB activity is dominant over dislocation mechanism at the high temperature, we can see more GB activity along with fewer dislocations. Therefore, we can state that it is possible to differentiate between the effects of the AIFs when both grain sizes and AIF thicknesses are different.

4.2.9. Deformation of NC Cu with AIF under creep

To understand the thermal stability and deformation behavior of the NC with the AIFs under a prolonged deformation process, we have performed a high-temperature creep test on our model. Again, for this simulation test, we have chosen a grain size of 11 nm. As for the parameters, we have used a high-temperature of 800 K, deformed them under the constant pressure of 0.5 GPa and let the deformation process run for 25 ns. From Figure 4-8 (b) and (c), we can distinguish between the effect of having the AIF. Figure 4-8 (b) exhibits the pure NC Cu sample before and after the deformation process. We can see that after 25 ns of constant deformation, not only dislocations can be found, but also the grain shapes have deformed completely due to grain growth. It is anticipated that under constant deformation at high-temperature, NC Cu will go through severe plastic deformation. However, from the figure (c), which show the NC Cu with the AIF of 1.0 nm, even after 25 ns tensile loading on it, neither it has shown any deformation nor any grain growth. Furthermore, the grain shapes have entirely retained their position. Therefore, it can be stated that using the AIF, under the high-temperature and prolonged deformation process, we can overcome the effect of grain growth in NC Cu material.

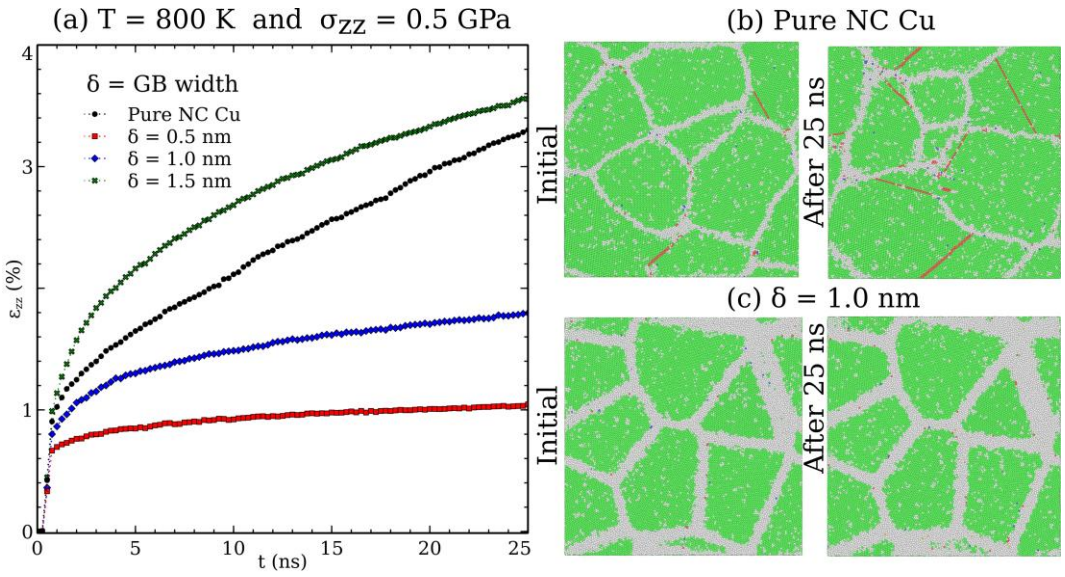

Figure 4-8: (a) Strain vs. time curve for the grain size of 11 nm with pure GB and AIF thickness of 0.5 nm to 1.5 nm; (b) Pure NC Cu models before and after the creep test; (c) AIF of 1. 0 nm before and after the creep test. Here, according to common neighbour analysis, green colored atoms stand for face-centered cubic structure and white colored atoms stand for unknown coordination structure.

Again, to confirm the characteristics of these models, we have completed the creep test on all our models and saw the differences in the Figure 4-8 (a). For both AIFs thicknesses of 0.5 nm and 1.0 nm, the strain has been reached only 0.9% and 1.5% respectively. On the contrary, it might be interesting to find that, for the AIF thickness of 1.5 nm, a much higher deformation has been observed, which is more than the pure NC Cu. The reason behind this characteristic is that 1.5 nm AIF NC Cu contains a more significant portion of amorphous atoms in their GB region which leads to a more substantial portion out of all atoms in the model. This model contains almost 47% of atoms consisted of the AIF portion. The amorphous material becomes very soft at high-temperature, and so, after this prolonged deformation process, it is very likely to see a

higher deformation in the end.

However, it is important to mention that, even after this much high strain, we do not see any dislocation activity which is undoubtedly due to the presence of AIF in the GB region. So, the deformation is no longer governed by the dislocations anymore.

4.3. Comparison of NW with AIF strength between literature and our work

Finally, to compare our results with previous literature results, especially for the direct comparison with the work from Rupert et al. [19] , we have made a NW out of our 3D NC Cu containing the AIF with a diameter of 20 nm. There are two reasons behind the selection; firstly, in MD, it is computationally challenging to run the simulation of our 3D models till fracture. Secondly, we have results from the literature of NW Cu with AIF to compare our results with previous ones. Then, we have chosen 100 K as our temperature in this simulation to continue our previous work. After that, we have performed the same tensile test until fracture on this simulation model with the grain size of 11 nm. We have applied a strain of 10^8/s in the z-direction of the model.

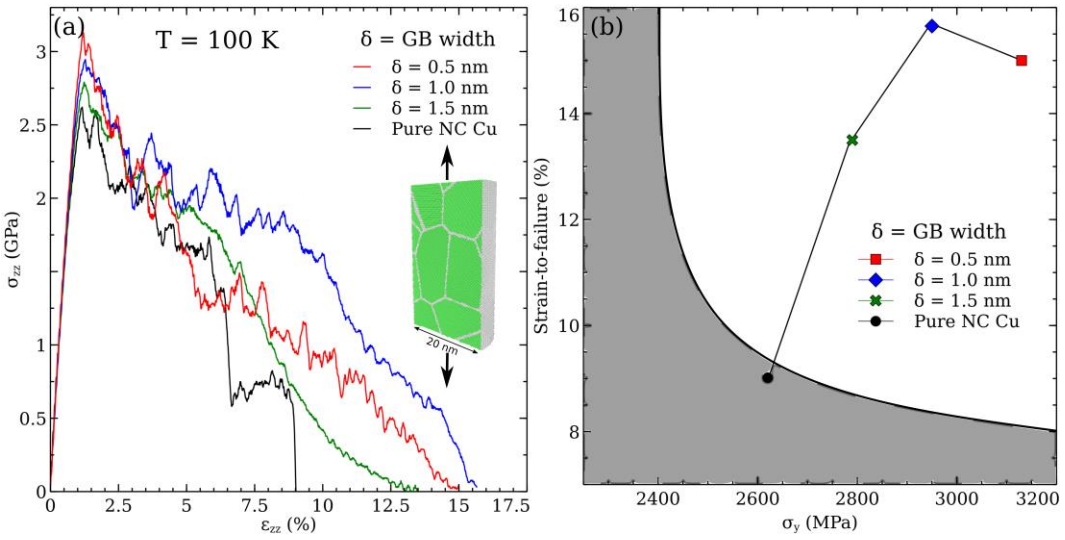

Figure 4-9: (a) Stress-strain curve of NC Cu NW with a grain diameter of 20 nm. Pure Cu GBs have been substituted with the AIFs and varying the AIFs thicknesses from 0.5 nm to 1.5 nm at 100 K. (b) Strain-to-failure vs. stress or toughness curve for the same models. All the previous mechanical loading results on Cu, Cu alloys fall in the filled grey region. Here, according to common neighbour analysis, green colored atoms stand for face-centered cubic structure and white colored atoms stand for unknown coordination structure.

In Figure 4-9 (a), we can see the stress-strain curve from this tensile test. For the pure NC Cu that it has deformed completely and fractured at the end with a strain of 9.5%. On the other hand, for the simulation models with the AIF, we do see different results. Although all of them have fractured at the end of the deformation process, the strain percentage is much higher compared to pure NC Cu NW. Among these three AIFs thicknesses, AIF 1.0 nm show the highest strain followed by AIF of 0.5 nm and 1.5 nm.

From the Figure 4-9 (a), we have extracted the area under the curve for all the simulation models and put the values in table 1.

Table 1: Values of toughness of Cu NW with different AIFs

GB thickness (nm)	Toughness ($x10^9$) ($J\text{-}m^{-3}$)
0.5	19
1.0	24.5
1.5	17
NC Cu	13.75

From table 1, we can clearly see the difference in the toughness values from our models. Pure NC Cu NW shows the lowest toughness value whereas, Cu NW with 1.0 nm AIF shows

the highest toughness among all of them followed by 0.5 nm and 1.5 nm AIFs thicknesses.

Lastly, to verify our results with the literature [19], we have compared the values between strain-to-failure with yield strength. Figure 4-9 (b) shows the strain-to-failure vs. yield stress of our simulation models. As consistent with the previous results, when the AIF thickness is 1.0 nm, we see the highest strength, as well as ductility, has been achieved. If we compare this data with the work of Rupert et al.[19], we find that our models are consistent with their work in terms of toughness. Not only that, by varying the AIF thickness, we have obtained higher strength compared to the previous work. Moreover, it might seem that the overall ductility is lower in our models compared to other literature reports; especially for pure Cu ones, it is important to mention that our simulation temperature was only 100 K. It has been already reported the effect of lower temperature that it decreases the overall ductility of NWs. [109]–[112]

Lastly, it has been the long-term drawback of the NC metals that they show a trade-off between strength and ductility. But we have shown that by creating AIF instead of pure GB in NC metals, it is possible to obtain both higher strength and ductility, *i.e.*, a high toughness material.

CHAPTER 5 Conclusions and Recommendations

5.1 Main findings and concluding remarks

The purpose of this research was to explore the effect of AIF in the Cu-Zr system, specially in the bulk material. The following studies have been carried out in this research with MD simulations:

- The influence of AIF in the interface energy of bi-crystal Cu.
- The influence of AIF in bi-crystal Cu under shear loading.
- Study of size dependent strength in NC Cu with the variation in thicknesses of AIFs.
- Study of deformation mechanism of NC Cu with the presence of AIF both at lower and higher temperatures.
- Toughness test of NW with the AIF.

Based on these studies, the following findings has been found:

- The AIF has a significant role in the interface energy. While the GB energy depends on the orientation of the interface, by introducing the AIF, energy values fall in a close range instead of a scattered one. Therefore, we can say the AIF reduce the interface energy, and orientation dependence is not observed anymore.
- Sliding is observed for the pure bi-crystal Cu.
- Strong dependence on the grain sizes and AIFs thicknesses have been observed at both lower and higher temperature.
- Due to the presence of AIF, deformation behavior of NC Cu with AIF have inclined more to GB activity rather than conventional dislocation mechanism.

- After the high-temperature creep test, NC Cu with AIF retain their grain shapes due to the presence of the AIF and thermal stability has been observed.
- From the tensile test of NC Cu NW, we do find that by including the AIF, not only the strength of the models have increased, but also we see a higher ductility.
- Finally, among all the AIF thicknesses, we do find that, for an optimum size of 1.0 nm, the NC Cu materials with the AIF exhibit superior material property.

Considering the research hypotheses in section 1.3, the concluding remarks are stated as follows:

- It was found that the presence of AIF makes the mateial relatively homogenous in terms of interface energy and orientation dependence can not be observed anymore.
- A strong influence of the grain sizes and AIF thicknesses was found in the strength of materials causing a shift in the strongest grain size to a larger size. Moreover, high toughness has been confirmed due to the presence of AIF which is consistent with the previous experimental results.
- It was also found that AIF can play a key role in the thermal stability of the NC material. Furthermore, a change in the deformation physics due to effect of AIF has been found shifting from dislocation mechanism to GB activity.

5.2 Recommendations for future works

The future work of this study will be focused on:

- Study the crack propagation of NC materials with the presence of AIF.
- Investigate the effect of AIF in NC materials under shock.

Based on the work presented in this thesis, one conference talk and one journal manuscript (to be submitted) have been produced.

- *Size-dependent strength and plasticity in nanocrystalline metal with amorphous grain boundary*, Afzal Hossain Neelav and Chuang Deng, TMS 2018, Phoenix, AZ, USA.
- *Size-dependent plasticity in nanocrystalline metals with amorphous complexion*, Afzal Hossain Neelav and Chuang Deng, manuscript in preparation.

Bibliography

[1] H. A. Padilla and B. L. Boyce, “A Review of fatigue behavior in nanocrystalline metals,” *Exp. Mech.*, vol. 50, no. 1, pp. 5–23, 2010.

[2] H. Gleiter, “Nanocrystalline Materials,” *Adv. Structural and Functional Materials*, vol. 33, pp. 223–315, 1990.

[3] G. Palumbo, S. J. Thorpe, and K. T. Aust, “On the contribution of triple junctions to the structure and properties of nanocrystalline materials,” *Scr. Metall. Mater.*, vol. 24, no. 7, pp. 1347–1350, 1990.

[4] S. J. Fensin, E. K. Cerreta, G. T. G. Iii, and S. M. Valone, “Why are some Interfaces in Materials Stronger than others ?," *Scientific Reports* volume 4, Article number: 5461 (2014), 2014.

[5] V. Y. Gertsman and K. Tangri, “Computer simulation study of grain boundary and triple junction distributions in microstructures formed by multiple twinning,” *Acta Metall. Mater.*, vol. 43, no. 6, pp. 2317–2324, 1995.

[6] B. L. Adams, “Orientation imaging microscopy: application to the measurement of grain boundary structure,” *Mater. Sci. Eng. A*, vol. 166, no. 1–2, pp. 59–66, 1993.

[7] P. G. Sanders, J. A. Eastman, and J. R. Weertman, “Elastic and tensile behavior of nanocrystalline copper and palladium,” *Acta Mater.*, vol. 45, no. 10, pp. 4019–4025, 1997.

[8] C. A. Schuh, T. G. Nieh, and H. Iwasaki, “The effect of solid solution W additions on the mechanical properties of nanocrystalline Ni,” *Acta Mater.*, vol. 51, no. 2, pp. 431–443, 2003.

[9] H. Conrad and J. Narayan, “Mechanism for grain size softening in nanocrystalline Zn,” *Appl. Phys. Lett.*, vol. 81, no. 12, pp. 2241–2243, 2002.

[10] S. R. Agnew, B. R. Elliott, C. J. Youngdahl, K. J. Hemker, and J. R. Weertman, "Microstructure and mechanical behavior of nanocrystalline metals," *Mater. Sci. Eng. A*, vol. A285, pp. 391–396, 2000.

[11] H. Van Swygenhoven and J. R. Weertman, "Deformation in nanocrystalline metals," *Mater. Today*, vol. 9, no. 5, pp. 24–31, 2006.

[12] K. J. Hemker et al. "Microstructural evolution in passivated Al films on Si substrates during thermal cycling," *Acta Materialia*, vol. 304, no. April, pp. 9–10, 2002.

[13] T. R. Bieler *et al.*, "The role of heterogeneous deformation on damage nucleation at grain boundaries in single phase metals," *Int. J. Plast.*, vol. 25, no. 9, pp. 1655–1683, 2009.

[14] T. R. Bieler, P. Eisenlohr, C. Zhang, H. J. Phukan, and M. A. Crimp, "Grain boundaries and interfaces in slip transfer," *Curr. Opin. Solid State Mater. Sci.*, vol. 18, no. 4, pp. 212–226, 2014.

[15] Z. Pan and T. J. Rupert, "Amorphous intergranular films as toughening structural features," *Acta Mater.*, vol. 89, pp. 205–214, 2015.

[16] Z. Pan and T. J. Rupert, "ScienceDirect Amorphous intergranular films as toughening structural features," *Acta Mater.*, vol. 89, pp. 205–214, 2015.

[17] T. J. Rupert, "The role of complexions in metallic nano-grain stability and deformation," *Curr. Opin. Solid State Mater. Sci.*, vol. 20, no. 5, pp. 257–267, 2016.

[18] P. R. Cantwell, M. Tang, S. J. Dillon, J. Luo, G. S. Rohrer, and M. P. Harmer, "Grain boundary complexions," *Acta Mater.*, vol. 62, no. 1, pp. 1–48, 2014.

[19] A. Khalajhedayati, Z. Pan, and T. J. Rupert, "Manipulating the interfacial structure of nanomaterials to achieve a unique combination of strength and ductility.," *Nat. Commun.*, vol. 7, p. 10802, 2016.

[20] J. L. Hirth, J P, *Theory of dislocations*. Krieger Publishing Company, 1982.

[21] L. Priester, *Grain boundaries and crystalline plasticity*. John Wiley & Sons, 2013.

[22] J. W. Cahn, "Transitions and Phase Equilibria Among Grain Boundary Structures," *Le J. Phys. Colloq.*, vol. 43, no. C6, pp. C6-199-C6-213, 1982.

[23] F. C. Frank, "Orientation mapping," *Metall. Trans. A*, vol. 19, no. 3, pp. 403–408, 1988.

[24] G. Gottstein and L. S. Shvindlerman, *Grain boundary migration in metals*. Boca Raton: CRC Press, 1999.

[25] H. A. Padilla, B. L. Boyce, C. C. Battaile, and S. V. Prasad, "Frictional performance and near-surface evolution of nanocrystalline Ni-Fe as governed by contact stress and sliding velocity," *Wear*, vol. 297, no. 1–2, pp. 860–871, 2013.

[26] T. J. Rupert, W. Cai, and C. A. Schuh, "Abrasive wear response of nanocrystalline Ni-W alloys across the Hall-Petchbreakdown," *Wear*, vol. 298–299, no. 1, pp. 120–126, 2013.

[27] K. Maung, J. C. Earthman, and F. A. Mohamed, "Inverse Hall-Petch behavior in diamantane stabilized bulk nanocrystalline aluminum," *Acta Mater.*, vol. 60, no. 16, pp. 5850–5857, 2012.

[28] J. R. Weertman, "T he Pursuit of the Small : From Grain- Nanocrystalline Metals," *MRS Bulletin*, Volume 29, Issue 9, pp. 616–620, 2004.

[29] H. Gleiter, "Nanostructured materials: basic concepts and microstructure," *Acta Mater.*, vol. 48, no. 1, pp. 1–29, 2000.

[30] R. Birringer, "Nanocrystalline Materials," *Materials Science and Engineering: A* vol. 117, pp. 33–43, 1989.

[31] M. A. Meyers, A. Mishra, and D. J. Benson, "Mechanical properties of nanocrystalline materials," *Progress in Materials Science* vol. 51, Issue 4, pp. 427–556, 2006.

[32] J. D. Eshelby, F. C. Frank, and F. R. N. Nabarro, "XLI. The equilibrium of linear arrays of

dislocations.," *London, Edinburgh, Dublin Philos. Mag. J. Sci.*, vol. 42, no. 327, pp. 351–364, 1951.

[33] E O Hall, "The Deformation and Ageing of Mild Steel: III Discussion of Results," *Proceedings of the Physical Society*, Section B, Volume 64, Number 9, 1951.

[34] J. Schiotz and K. W. Jacobsen, "A maximum in the strength of nanocrystalline copper," *Science*, vol. 301, no. 5638, pp. 1357–1359, 2003.

[35] E. Ma, "Instabilities and ductility of nanocrystalline and ultrafine-grained metals," *Scr. Mater.*, vol. 49, no. 7, pp. 663–668, 2003.

[36] T. G. Nieh and J. Wadsworth, "Hall-petch relation in nanocrystalline solids," *Scr. Metall. Mater.*, vol. 25, no. 4, pp. 955–958, 1991.

[37] R. W. Siegel and G. J. Thomas, "Grain boundaries in nanophase materials," *Ultramicroscopy*, vol. 40, no. 3, pp. 376–384, 1992.

[38] C. S. Pande and K. P. Cooper, "Nanomechanics of Hall-Petch relationship in nanocrystalline materials," *Prog. Mater. Sci.*, vol. 54, no. 6, pp. 689–706, 2009.

[39] C. A. Schuh, T. G. Nieh, and T. Yamasaki, "Hall-Petch breakdown manifested in abrasive wear resistance of nanocrystalline nickel," *Scr. Mater.*, vol. 46, no. 10, pp. 735–740, 2002.

[40] C. C. Koch, D. G. Morris, K. Lu, and A. Inoue, "Ductility of bulk nanostructured materials.," *Scitech B. News*, vol. 34, no. 3, pp. 54–58, 2010.

[41] F. D. Di Tolla and K. W. Jacobsen, "Softening of nanocrystalline metals at very small grain sizes," *Nature*, vol. 391, no. February, pp. 561–563, 1998.

[42] H. Hahn, P. Mondal, and K. A. Padmanabhan, "Plastic deformation of nanocrystalline materials," *Nanostructured Mater.*, vol. 9, no. 1–8, pp. 603–606, 1997.

[43] H. Van Swygenhoven and P. M. Derlet, "Grain-boundary sliding in nanocrystalline fcc

metals," *Phys. Rev. B - Condens. Matter Mater. Phys.*, vol. 64, no. 22, pp. 1–9, 2001.

[44] D. Jia, K. T. Ramesh, and E. Ma, "Effects of nanocrystalline and ultrafine grain sizes on constitutive behavior and shear bands in iron," *Acta Mater.*, vol. 51, no. 12, pp. 3495–3509, 2003.

[45] Y. Wang, M. Chen, F. Zhou, and E. Ma, "High tensile ductility in a nanostructured metal," *Nature*, vol. 419, pp. 912–915, 2002.

[46] D. Jia, Y. M. Wang, K. T. Ramesh, E. Ma, Y. T. Zhu, and R. Z. Valiev, "Deformation behavior and plastic instabilities of ultrafine-grained titanium," *Appl. Phys. Lett.*, vol. 79, no. 5, pp. 611–613, 2001.

[47] L. Wang *et al.*, "Grain rotation mediated by grain boundary dislocations in nanocrystalline platinum," *Nat. Commun.*, vol. 5, pp. 1–7, 2014.

[48] V. Y. Gertsman and R. Birringer, "On the room-temperature grain growth in nanocrystalline copper," *Scr. Metall. Mater.*, vol. 30, no. 5, pp. 577–581, 1994.

[49] P. C. Rivas, M. C. Caracoche, R. Caruso, N. Pellegri, O. De Sanctis, and I. Introduction, "*Materials research*," no. m, pp. 11–13, 2000.

[50] J. Eckert, J. Holzer C., C. III E.,Krill, W. Johnson L., C. Krill E., and W. Johnson L., "Structural and thermodynamic properties of nanocrystalline fcc metals prepared by mechanical attrition," *J. Mater. Res.*, vol. 7, no. 7, pp. 1751–1761, 1992.

[51] M. A. Tschopp, H. A. Murdoch, L. J. Kecskes, and K. A. Darling, "Bulk nanocrystalline metals: Review of the current state of the art and future opportunities for copper and copper alloys," *Jom*, vol. 66, no. 6, pp. 1000–1019, 2014.

[52] J. Weissrmiller, "Alloy effects in nanostructures," *Nanostructured Materials*, Vol 3, Issue 1-6, Pages 261-272, 1993.

[53] J. Weissmüller, “Alloy effects in nanostructures,” *Nanostructured Mater.*, vol. 3, no. 1–6, pp. 261–272, 1993.

[54] M. Saber, H. Kotan, C. C. Koch, and R. O. Scattergood, “Thermodynamic stabilization of nanocrystalline binary alloys,” *J. Appl. Phys.*, vol. 113, no. 6, 2013.

[55] N. Zhou and J. Luo, “Developing thermodynamic stability diagrams for equilibrium-grain-size binary alloys,” *Mater. Lett.*, vol. 115, pp. 268–271, 2014.

[56] P. R. Cantwell, M. Tang, S. J. Dillon, J. Luo, G. S. Rohrer, and M. P. Harmer, “ScienceDirect Grain boundary complexions,” *Acta Mater.*, vol. 62, no. 152, pp. 1–48, 2013.

[57] D. McLean, “Grain boundaries in metals’; 1957,” *London, Oxford Univ. Press.*

[58] S. J. Dillon, M. Tang, W. C. Carter, and M. P. Harmer, “Complexion: A new concept for kinetic engineering in materials science,” *Acta Mater.*, vol. 55, no. 18, pp. 6208–6218, 2007.

[59] J. Luo, H. Cheng, K. M. Asl, C. J. Kiely, and M. P. Harmer, “The role of a bilayer interfacial phase on liquid metal embrittlement,” *Science*, vol. 333, no. 6050, pp. 1730–1733, 2011.

[60] Y. Wang, J. Li, A. V Hamza, and T. W. Barbee, “Ductile crystalline-amorphous nanolaminates.,” *Proc. Natl. Acad. Sci. U. S. A.*, vol. 104, no. 27, pp. 11155–60, 2007.

[61] Y. M. Wang, A. V. Hamza, and T. W. Barbee, “Incipient plasticity in metallic glass modulated nanolaminates,” *Appl. Phys. Lett.*, vol. 91, no. 6, pp. 1–4, 2007.

[62] C. Brandl, T. C. Germann, and A. Misra, “Structure and shear deformation of metallic crystalline-amorphous interfaces,” *Acta Mater.*, vol. 61, no. 10, pp. 3600–3611, 2013.

[63] M. L. Falk, “Simulations of shear banding in metallic glasses.” American Physical Society, 2008 APS March Meeting, March 10-14, 2008, abstract id. S3.002, 2008.

[64] H. A. Murdoch and C. A. Schuh, “Estimation of grain boundary segregation enthalpy and

its role in stable nanocrystalline alloy design," *J. Mater. Res.*, vol. 28, no. 16, pp. 2154–2163, 2013.

[65] H. Men, Z. Q. Hu, and J. Xu, "Bulk metallic glass formation in the Mg–Cu–Zn–Y system," *Scr. Mater.*, vol. 46, no. 10, pp. 699–703, 2002.

[66] Y. Mishin, M. Asta, and J. Li, "Atomistic modeling of interfaces and their impact on microstructure and properties," *Acta Mater.*, vol. 58, no. 4, pp. 1117–1151, 2010.

[67] Y. T. Zhu, X. Z. Liao, and X. L. Wu, "Deformation twinning in nanocrystalline materials," *Prog. Mater. Sci.*, vol. 57, no. 1, pp. 1–62, 2012.

[68] A. Khalajhedayati and T. J. Rupert, "High-Temperature Stability and Grain Boundary Complexion Formation in a Nanocrystalline Cu-Zr Alloy," *Journal of Materials*, vol. 67, no. 12, pp. 2788–2801, 2015.

[69] V. Turlo and T. J. Rupert, "Grain boundary complexions and the strength of nanocrystalline metals: Dislocation emission and propagation," *Acta Mater.*, vol. 151, pp. 100–111, 2018.

[70] M. P. Allen, "Introduction to Molecular Dynamics Simulation," *Computational Soft Matter: From Synthetic Polymers to Proteins*, vol. 23, 2004.

[71] D. Frenkel, "Understanding Molecular Simulation." *Computational Science Serie*, Vol 1, 1996

[72] G. Makov and M. C. Payne, "Periodic boundary conditions in ab initio calculations," *Physical Review B*, vol. 51, no. 7. pp. 4014–4022, 1995.

[73] Murray S. Daw and I. Baskes, "Embedded-atom method: Derivation and application to impurities, surfaces, and other defects in metals," *Physical Review B*, vol. 29, no. 12, 1984.

[74] Y. Mishin, "Structural stability and lattice defects in copper : Ab initio , tight-binding , and embedded-atom calculations," *Physical Review B*, vol. 63, pp. 1–16, 2001.

[75] M. I. Mendelev, M. J. Kramer, C. A. Becker, and M. Asta, “Analysis of semi-empirical interatomic potentials appropriate for simulation of crystalline and liquid Al and Cu,” *Philosophical Magazine*, vol. 88, Issue 12, 2008.

[76] M. I. Mendelev, D. J. Sordelet, M. J. Kramer, M. I. Mendelev, D. J. Sordelet, and M. J. Kramer, “Using atomistic computer simulations to analyze x-ray diffraction data from metallic glasses Using atomistic computer simulations to analyze x-ray diffraction,” *Journal of Applied Physics*, vol. 043501, no. 2007, 2017.

[77] Y. Q. Cheng and E. Ma, “Atomic-level structure and structure-property relationship in metallic glasses,” *Prog. Mater. Sci.*, vol. 56, no. 4, pp. 379–473, 2011.

[78] C. A. Schuh, T. C. Hufnagel, and U. Ramamurty, “Mechanical behavior of amorphous alloys,” *Acta Mater.*, vol. 55, no. 12, pp. 4067–4109, 2007.

[79] S. Pauly, S. Gorantla, G. Wang, U. Kühn, and J. Eckert, “Transformation-mediated ductility in CuZr-based bulk metallic glasses,” *Nat. Mater.*, vol. 9, no. 6, pp. 473–477, 2010.

[80] K. Albe, Y. Ritter, and D. Şopu, “Enhancing the plasticity of metallic glasses: Shear band formation, nanocomposites and nanoglasses investigated by molecular dynamics simulations,” *Mech. Mater.*, vol. 67, pp. 94–103, 2013.

[81] M. I. Mendelev, D. J. Sordelet, and M. J. Kramer, “Using atomistic computer simulations to analyze x-ray diffraction data from metallic glasses,” *J. Appl. Phys.*, vol. 102, no. 4, 2007.

[82] G. Duan *et al.*, “Molecular dynamics study of the binary Cu46Zr54 metallic glass motivated by experiments: Glass formation and atomic-level structure,” *Phys. Rev. B - Condens. Matter Mater. Phys.*, vol. 71, no. 22, pp. 1–9, 2005.

[83] D. Turnbull, “Under what conditions can a glass be formed?,” *Contemp. Phys.*, vol. 10, no. 5, pp. 473–488, 1969.

[84] W. H. Wang, C. Dong, and C. H. Shek, “Bulk metallic glasses,” *Mater. Sci. Eng. R Reports*, vol. 44, no. 2–3, pp. 45–90, 2004.

[85] D. J. Srolovitz, T. Egami, V. Vitek, D. Srolovitz, T. Egami, and V. Vitek, “Radial Distribution Function and Structural Relaxation in Amorphous Solids,” *Phyiscal Rev. B*, vol. 24, no. 12, pp. 6936–6944, 1981.

[86] H. W. Sheng, W. K. Luo, F. M. Alamgir, J. M. Bai, and E. Ma, “Atomic packing and short-to-medium-range order in metallic glasses.,” *Nature*, vol. 439, no. 7075, pp. 419–425, 2006.

[87] D. B. Miracle, “A structural model for metallic glasses,” *Nat. Mater.*, vol. 3, no. 10, pp. 697–702, 2004.

[88] P. Hirel, “Atomsk: A tool for manipulating and converting atomic data files,” *Comput. Phys. Commun.*, vol. 197, pp. 212–219, 2015.

[89] M. Parrinello and A. Rahman, “Polymorphic transitions in single crystals : A new molecular dynamics method Polymorphic transitions in single crystals : A new molecular dynamics method,” *J. Appl. Phys.*, vol. 7182, no. 1981, 2005.

[90] M. Parrinello and A. Rahman, “Polymorphic transitions in single crystals: A new molecular dynamics method,” *J. Appl. Phys.*, vol. 52, no. 12, pp. 7182–7190, 1981.

[91] D. Faken and H. Jónsson, “Systematic analysis of local atomic structure combined with 3D computer graphics,” *Comput. Mater. Sci.*, vol. 2, no. 2, pp. 279–286, 1994.

[92] M. L. Falk and J. S. Langer, “Dynamics of viscoplastic deformation in amorphous solids,” *Phys. Rev. E - Stat. Physics, Plasmas, Fluids, Relat. Interdiscip. Top.*, vol. 57, no. 6, pp. 7192–7205, 1998.

[93] F. Shimizu, S. Ogata, and J. Li, “Theory of Shear Banding in Metallic Glasses and Molecular Dynamics Calculations,” *Mater. Trans.*, vol. 48, no. 11, pp. 2923–2927, 2007.

[94] M. A. Tschopp and D. L. McDowell, “Influence of single crystal orientation on homogeneous dislocation nucleation under uniaxial loading,” *J. Mech. Phys. Solids*, vol. 56, no. 5, pp. 1806–1830, 2008.

[95] D. L. Olmsted, S. M. Foiles, and E. A. Holm, “Survey of computed grain boundary properties in face-centered cubic metals: I. Grain boundary energy,” *Acta Mater.*, vol. 57, no. 13, pp. 3694–3703, 2009.

[96] M. A. Tschopp, K. N. Solanki, F. Gao, X. Sun, M. A. Khaleel, and M. F. Horstemeyer, “Probing grain boundary sink strength at the nanoscale: Energetics and length scales of vacancy and interstitial absorption by grain boundaries in α-Fe,” *Phys. Rev. B - Condens. Matter Mater. Phys.*, vol. 85, no. 6, pp. 1–21, 2012.

[97] M. A. Tschopp, D. E. Spearot, and D. L. McDowell, “Atomistic simulations of homogeneous dislocation nucleation in single crystal copper,” *Model. Simul. Mater. Sci. Eng.*, vol. 15, no. 7, pp. 693–709, 2007.

[98] M. A. Tschopp and D. L. McDowell, “Asymmetric tilt grain boundary structure and energy in copper and aluminium,” *Philos. Mag.*, vol. 87, no. 25, pp. 3871–3892, 2007.

[99] D. Wolf, “Structure-energy correlation for grain boundaries in F.C.C. metals-III. Symmetrical tilt boundaries,” *Acta Metall. Mater.*, vol. 38, no. 5, pp. 781–790, 1990.

[100] D. Wolf, “A read-shockley model for high-angle grain boundaries,” *Scr. Metall.*, vol. 23, no. 10, pp. 1713–1718, 1989.

[101] J. M. Zhang, X. M. Wei, and H. Xin, “Energy analysis for (1 1 1) twist grain boundary in noble metals,” *Appl. Surf. Sci.*, vol. 243, no. 1–4, pp. 1–6, 2005.

[102] D. Wolf, “Structure-energy correlation for grain boundaries in F.C.C. metals-I. Boundaries on the (111) and (100) planes,” *Acta Metall.*, vol. 37, no. 7, pp. 1983–1993, 1989.

[103] F. Sansoz and J. F. Molinari, "Mechanical behavior of Σ5 tilt grain boundaries in nanoscale Cu and Al: A quasicontinuum study," *Acta Mater.*, vol. 53, no. 7, pp. 1931–1944, 2005.

[104] Y. Wei, C. Su, and L. Anand, "A computational study of the mechanical behavior of nanocrystalline fcc metals," *Acta Mater.*, vol. 54, no. 12, pp. 3177–3190, 2006.

[105] M. Dao, L. Lu, R. J. Asaro, J. T. M. De Hosson, and E. Ma, "Toward a quantitative understanding of mechanical behavior of nanocrystalline metals," *Acta Mater.*, vol. 55, no. 12, pp. 4041–4065, 2007.

[106] F. Sansoz and J. F. Molinari, "Incidence of atom shuffling on the shear and decohesion behavior of a symmetric tilt grain boundary in copper," *Scr. Mater.*, vol. 50, no. 10, pp. 1283–1288, 2004.

[107] J. Schiøtz, "Atomic-scale modeling of plastic deformation of nanocrystalline copper," *Scr. Mater.*, vol. 51, no. 8 SPEC. ISS., pp. 837–841, 2004.

[108] K. M. Youssef, R. O. Scattergood, K. L. Murty, J. A. Horton, and C. C. Koch, "Ultrahigh strength and high ductility of bulk nanocrystalline copper," *Appl. Phys. Lett.*, vol. 87, no. 9, pp. 1–3, 2005.

[109] S. J. A. Koh, H. P. Lee, C. Lu, and Q. H. Cheng, "Molecular dynamics simulation of a solid platinum nanowire under uniaxial tensile strain: Temperature and strain-rate effects," *Phys. Rev. B - Condens. Matter Mater. Phys.*, vol. 72, no. 8, pp. 1–11, 2005.

[110] S. J. A. Koh and H. P. Lee, "Molecular dynamics simulation of size and strain rate dependent mechanical response of FCC metallic nanowires," *Nanotechnology*, vol. 17, no. 14, pp. 3451–3467, 2006.

[111] H. A. Wu, "Molecular dynamics study of the mechanics of metal nanowires at finite temperature," *Eur. J. Mech. - A/Solids*, vol. 25, no. 2, pp. 370–377, 2006.

[112] J.-W. Kang and H.-J. Hwang, “Mechanical deformation study of copper nanowires using atomistic simulation,” *Nanotechnology*, vol. 12, pp. 295–300, 2001.